Dynamic Optical Metamaterials Based on Vanadium Dioxide

by

Zhihua Zhu

Dissertation

Submitted to the Faculty of the

Graduate School of Vanderbilt University

in partial fulfillment of the requirements

for the degree of

DOCTOR OF PHILOSOPHY

in

Electrical Engineering

January 31, 2019

Nashville, Tennessee

Approved:

Jason G. Valentine, Ph.D.

Richard F. Haglund Jr. Ph.D.

Sharon M. Weiss, Ph.D.

Joshua D. Caldwell, Ph.D.

Justus C. Ndukaife, Ph.D

I dedicate this work to my parents.

ACKNOWLEDGEMENTS

My thanks are due first and foremost to my PhD advisor, Jason Valentine, for his continuous guidance and tremendous support through my graduate career. What I have learned from Prof. Valentine is not only that he is knowledgeable and full of insights about the field; more important is the attitude he has shown me as a critical and independent researcher. As an advisor, he always encourages us to think systematically what really matters practically, how to fundamentally solve the problems, and then how to write scientific papers to spread our ideas. He is always open for discussion and tells us "just stop by his office" anytime we have questions and problems. Prof. Valentine is also very patient mentor. He derives equations together with us, trains us how to handle the laser and use the darkroom hand by hand, corrects our grammar errors in writing, and so on. Those memories are indeed the precious fortune in my life. He also encourages us to attend research conferences, sharpen our presenting skills and build social networks. In my search for careers, he also helps me a lot, giving me very good suggestions and preparing me well for all of the interviews.

I would like to thank my other research advisor Prof. Richard Haglund for his kind guidance and continuous support in my research. Prof. Haglund is energetic with broad scientific views. His insights are always very inspiring when I do not fully understand some concepts and results. He helps me to sort puzzles by recommending the right references when I get confused. Prof. Haglund is very supportive for collaborations with other research groups, which helps us to broad our research horizons. He is very active to arrange meetings with the invited seminar speakers on campus, encouraging us to communicate with them and seek for valuable suggestions. Prof. Haglund is also a good listener. When I get upset and frustrated, chatting with him heals a lot.

I would also like to thank Prof. Sharon Weiss, Prof. Joshua Caldwell, and Prof. Justus Ndukaife for serving on my dissertation committee, spending time and efforts reviewing my research projects, and supporting me with valuable suggestions.

I am grateful for my collaborators for helpful discussions about the project. I would like to

iii

thank Phil Evans from ORNL, Peter Liu from UB, Prof. Joyce Poon from the University of Toronto, and Zhe Cheng from G-Tech for sharing ideas with me and helping me to learn.

A very special gratitude goes out to all of the Valentine group and Haglund group members, both past and present. Their continuous help, patience and friendship have made my graduate career here productive and fun. These are the best memories I cherish for my whole life. Specially, I thank Wenyi, Rod and Bob for helping me to start, and thank Zack, Kevin, Austin, You, Claire, Kent Fabian, Sam, Jason, Christina and David for valuable discussions.

I also want thank all of the Caldwell group members for insightful discussions both in the group meetings and daily research life, with special thanks to Tom Folland, who has helped me so much with developing ideas and designing experiment. I am also very grateful to Enxia Zhang from the RER group. She has spent a lot of time teaching me wire bonding skill. She is also a good friend. She invites me to the RER group parties, which makes my graduate life in Vanderbilt colorful.

I want to especially thank all of the VINSE staff and CNMS staff who have helped me. Special thanks to Tomy Hmelo, Kurt Heinrich, Bo Choi, Ben Schmidt, Bill Martinez and Alice Leach for their patience and tolerance when I make trouble, and more importantly for all of the helpful suggestions they have given to me.

In addition, I want to thank all my friends in Nashville, especially to Kathy Liu, Angela Wang, Hua Li, Zhenfang Sun, Kate Hayes, Nathan Ives, Rong Jiang, Simeng Zhao, Pan Wang, Jing Fan, Jie Zhao who have shared a lot of time and memories with me. I also want to thank the NCCC dance group for welcoming in the team, teaching me how to dance and express myself.

Most importantly, I would like to thank my family. Thanks to my parents, grandparents, brother and sister-in-law for their unwaving support and love. I could not make it so far without your backup. Very special gratitude goes to my husband Huiqi Gong for your endless love and encouragement. You've made my life so special and I am the luckiest one to have you in my life.

TABLE OF CONTENTS

LIST OF TABLES

LIST OF FIGURES

CHAPTER 1 INTRODUCTION

In the history of science, the first application of an optical microscope to investigate Nature marked the beginning of a new era. The fascinating microscale features observed with this newly developed instrument were initially questioned but then accepted and interpreted by indirect measurement. With more and more understanding of the physical laws and relationships, scientists began to implement these features to engineer the light-matter interaction. Applications include, but are not limited to, ultrafast data transfer and storage, high efficiency energy conversion, enhanced biosensing, as well as precise manipulation of nanoscale objects.

Metamaterials are artificial materials with building blocks much smaller than the electromagnetic wavelength and can be treated as an effective medium. The interactions between this medium and the incident light can be harnessed by modifying the basic construction materials or the geometric shapes or dimensions of the structures. Metamaterials can be designed to realize many properties that do not exist in Nature, such as zero and negative refraction, cloaking, and superlensing. However, most of the past designs are passive that once made, the properties cannot be changed. Many applications require that the optical signal be modulated in real-time. To accomplish this, researchers have been combining these passive elements with functional matter, whose properties can be changed with external stimuli such as light, electrical or magnetic fields, chemicals, temperature, stress or pressure. This combination is referred to as tunable, dynamic, or reconfigurable metamaterials.

Based on the ease of fabrication, as well as the device yield, thick and continuous functional films such as indium tin oxide (ITO) layer and phase change materials are usually used in these reconfigurable systems. Drawbacks of this approach include large power consumption, suppressed rise and recovering speed, limited modulation depth, as well as reduced spatial resolution caused by nonradiative loss in the system. One solution to these issues is to reduce the effective volume of the active material while integrating the material in a region of field concentration region.

This solution will be the topic of this dissertation. Here, a phase change material, vanadium dioxide (VO_2), is used because of its near-room temperature phase transition threshold and large optical parameter contrast in the infrared region. By embedding low thermal mass VO_2 nanoparticles into a plasmonic bowtie concentrator or all dielectric Huygens metasurface, we have achieved complete control over the material absorption, reflection, and transmission at infrared wavelengths. This approach results in high-speed switching as well as a low power triggering threshold. Furthermore, this design could also be used for phase control and could be translated to visible or terahertz regimes.

This dissertation is organized as follows:

Chapter 2 first gives a detailed introduction to the working principle of metamaterials, basic composition, and the plasmonic and all-dielectric variants that can be used as electric field concentrators. This chapter also gives an overview of reconfigurable metamaterials, their current limitations and potential solutions.

Chapter 3 covers optical phase change materials, their applications, and the properties of VO_2 including as-deposited films and patterned nanoparticles with decreased dimensionality. The methods to characterize VO_2 properties are also presented here.

Chapter 4 demonstrates a near-infrared light modulator, assisted by plasmonic bowtie antenna and integrated with VO_2 nanostructures. With the help of local resistive heating, this device is able to realize 33% reflection/absorption modulation contrast, and 400 times faster recovering speed and 50 times lower operating power compared with continuous film designs. In this chapter we will also present one of the possible applications - security recognition and rewritable infrared displays.

Chapter 5 describes a near infrared optical limiter based on an all-dielectric Huygens metasurface. High-index silicon cylinders form Mie resonator cavities which are used to obtain high electric- and magnetic-field concentration inside of the cylinder. An epsilon-near-zero (ENZ)

material is introduced to better confine the electric field distribution. Based on the numerical simulations, we find that our results compare favorably with other optical limiters. We also carry out thermal steady-state analysis to estimate the switching threshold.

Chapter 6 summarizes the highlights of this work and its long-term perspectives. Future opportunities as well as challenges will also be discussed.

CHAPTER 2 BACKGROUND ON METAMATERIALS

2.1 Introduction of Metamaterials

As briefly mentioned in the introduction chapter, electromagnetic metamaterials refer to nanostructured composites that exhibit unique electromagnetic properties [1]. Different from the natural materials, the optical responses of metamaterials are not primarily dependent on the intrinsic properties of the chemical constituents, but rather on the specific geometry and dimensions of the structuring. These artificial structures function as artificial atoms and by engineering their optical response, they have the potential to fill critical voids in the electromagnetic spectrum, where material response is limited, and enable the construction of novel electromagnetic materials.

To better understand the light-matter interactions in metamaterials, we can begin with the Maxwell's equations, which define the fields generated by the charges and currents in the materials. In differential form and SI units the macroscopic Maxwell's equations have the form:

w
$$\nabla \cdot \vec{\mathbf{D}} = \rho,$$

$$\nabla \cdot \vec{\mathbf{B}} = 0,$$

$$\nabla \times \vec{\mathbf{E}} = -\frac{\partial \vec{\mathbf{B}}}{\partial t}, \tag{2.1}$$

$$\nabla \times \vec{\mathbf{H}} = \vec{\mathbf{j}} + \frac{\partial \vec{\mathbf{D}}}{\partial t}$$

where **E** denotes the electrical field, **H** the magnetic field, **D** the displacing currents, **B** the magnetic flux density, ρ is charge density and j is current density. From the constitutive relations, we have

$$\vec{\mathbf{D}} = \varepsilon_0 \varepsilon_r \vec{\mathbf{E}}$$

$$\vec{\mathbf{B}} = \varepsilon_0 \varepsilon_r \vec{\mathbf{H}} \tag{2.2}$$

4

Here $\varepsilon_0 = 8.85 \times 10^{-12}$ F/m is the permittivity of vacuum, and $\mu_0 = 1.26 \times 10^{-6}$ H/m is the vacuum permeability; electric permittivity ε_r is a measure of how the applied electric field interacts with the medium and permeability μ_r measures the response of a material to an applied magnetic field.

Combining equation (2.1) and (2.2), and assuming there are no surface currents or free charges, the wave equation can be derived as:

$$\nabla^2 \vec{\mathbf{E}} = \mu_0 \mu_r \varepsilon_0 \varepsilon_r \frac{\partial^2 \mathbf{E}}{\partial t^2},$$

(2.3)

$$\nabla^2 \vec{\mathbf{H}} = \mu_0 \mu_r \varepsilon_0 \varepsilon_r \frac{\partial^2 \mathbf{H}}{\partial t^2}$$

We can tell from equation (2.3) that as an electromagnetic wave, the propagation of light through an optical medium is dictated by the relative permittivity ε_r and permeability μ_r. These two parameters are generally fixed in natural materials; while for metamaterials they can be designed by changing the material composition, and more importantly by changing the geometry and structuring.
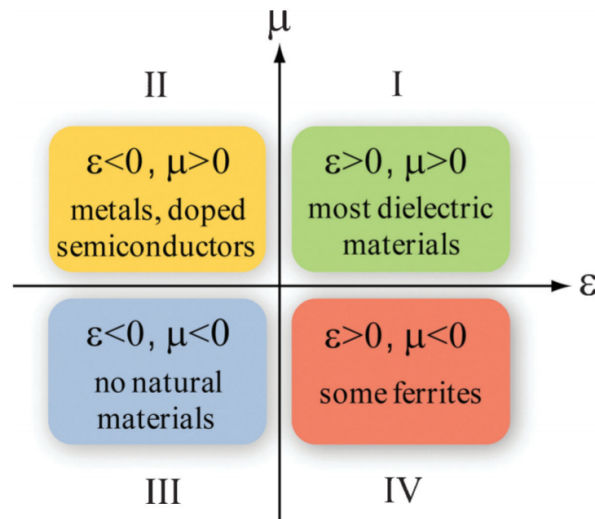
Figure 2.1 Material parameter space characterized by electric permittivity ε and magnetic permeability μ. [1]

A "materials parameter space" is plotted in Figure 2.1. Materials in region I-IV exist in nature and include dielectrics, metals to ferrites. Region III is occupied by metamaterials with simultaneously negative permittivity and permeability, which are referred to as "negative index materials (NIMs)" or "left handed materials (LHMs)". Engineering the effective permittivity is a long-known concept which can be obtained with diluted metals or artificial dielectrics, while engineering the magnetic response was proposed in 2000. A negative refractive index metamaterial was first theoretically analyzed and experimentally realized in the microwave region [2][3]. Driven by the miniaturization of the electronic circuits in the semiconductor industry, nanotechnology has allowed a dramatic development for metallic or all-dielectric metamaterials optical devices ddown to infrared and visible wavelengths.

2.2 Extreme Light Concentration in Metamaterials

Metamaterials mainly use the resonance behaviors of nanostructures to realize complete control over the optical parameters such as the effective permittivity and permeability. In metamaterials, the isolated unit cells act as optical cavities supported by the local collective motion of electrons in metal structure or trapping of the electromagnetic wave in high-index particles. The medium exhibits effective optical properties quite different from non-resonant condition, such as enhanced transmission or absorption, additional phase delay and altered polarization. In the near field, the incident electric and magnetic field can be concentrated in deep sub-wavelength volumes. These volumes can be much smaller than the free-space diffraction limit. The ability to manipulate the far and near-field of light has led to applications such as high spatial resolution imaging techniques[4]-[8], ultrasensitive photodetectors [9]-[12] and biosensing [13][14], ultrafast light modulators [15][16]and energy harvest and super-efficient solar cells [17]- [19].

2.1.1 Localized Surface Plasmon Resonance (LSPR)

A surface plasmon is a collective oscillation of the free electrons at a material surface, induced by the time-varying electric field associated with light waves incident on the surface. A very nice illustration of a plasmonic effect is colored glasses, for example the famous Lycurgus cup, which was made by ancient Roman artists and now exhibited in the British Museum in London. When illuminated by a white light source, the cup shows a red color in transmission and greenish color from the reflection side (Figure 2.2). Today this phenomenon has been well investigated, and attributed to scattering from the nanometer-sized gold/silver alloy particles embedded in the glass [20].
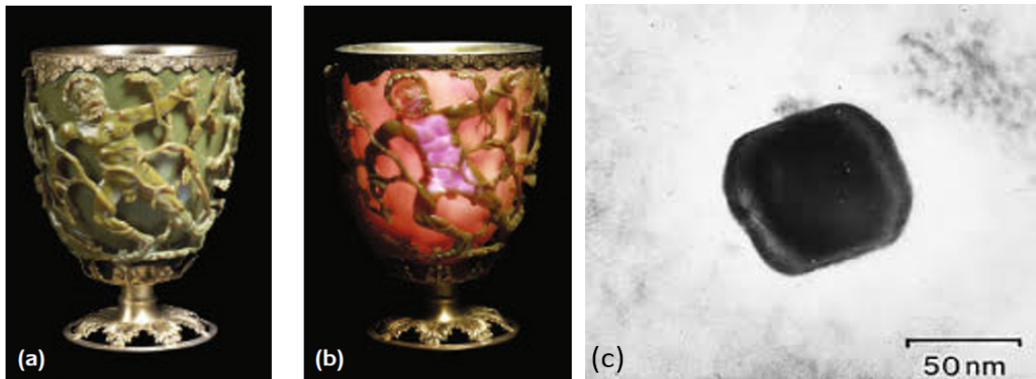
Figure 2.2 Ancient Lycurgus cup illuminated by a light source (a) outside and (b) inside the cup, respectively; (c) Transmission electron microscopy (TEM) image of a gold/silver alloy particle within the glass [20][21].

To excite surface plasmon in continuous metal films, additional optics like gratings or coupling prisms are needed to provide additional in-plane momentum. However, in metal nanostructures, the edges and boundaries scatter light, providing large momentum vectors and exciting a localized surface plasmon resonance (LSPR) without assistances from extra coupling optics. The LSPR is a plasmon bound state. Generally, the resonance frequency is a function of the shape, size and material of the nanostructure. The resonance spectral width, or full width at half

maximum (FWHM), is mainly dictated by the nonradiative and radiative loss in the systems. The nonradiative loss arises due to the imaginary part of the dielectric constant where larger loss results in a broader resonance [22].
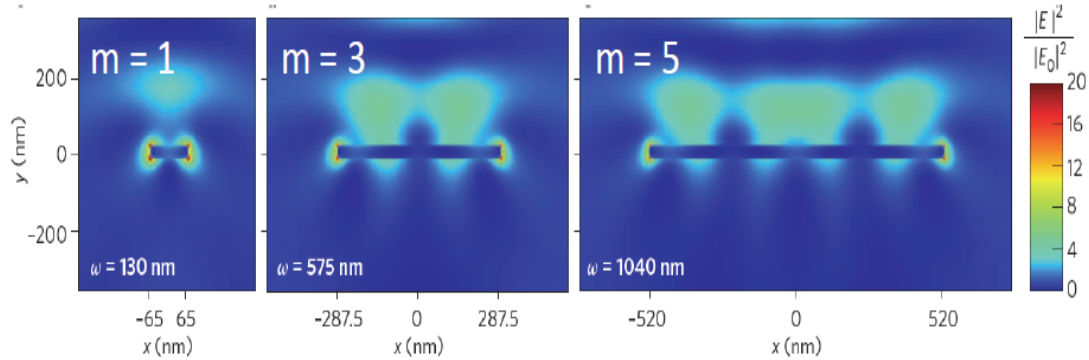
Figure 2.3 Normalized field intensity redistribution for resonances with orders (m=1, 3, 5). The resonator is silver strips with 30nm thickness and length w=130nm, 575nm, 1040nm, respectively. The illumination source is λ_0=550 nm [23].

When the incident wavelength is significantly larger than the particle size (quasistatic approximation), the resonance position is dictated solely by the dielectric constants of the metal and surrounding materials and the electric field is constant across the whole particle at any instant of time. In the non-quasistatic regime, the nanostructure dimension parallel to the incoming electric field is comparable to the incident wavelength. In this case, the field distribution cannot be treated as uniform in the unit cell. This critical dimension plays a very important role in the field redistribution, as seen in Figure 2.3 [23].

When an LSPR is excited, surface plasmon polaritons (SPPs) propagate back and forth between the two sides of the silver antenna, forming a Fabry-Perot resonator. At resonance the length of such antenna is equal to $m\lambda_{SPP}/2$, where m is an integer and λ_{SPP} is the wavelength of

the supported SPP mode. From the normalized electric field distribution in Figure 2.3, it is observed that the electric field node numbers are 2, 4 and 6, and at each node the field is greatly enhanced.
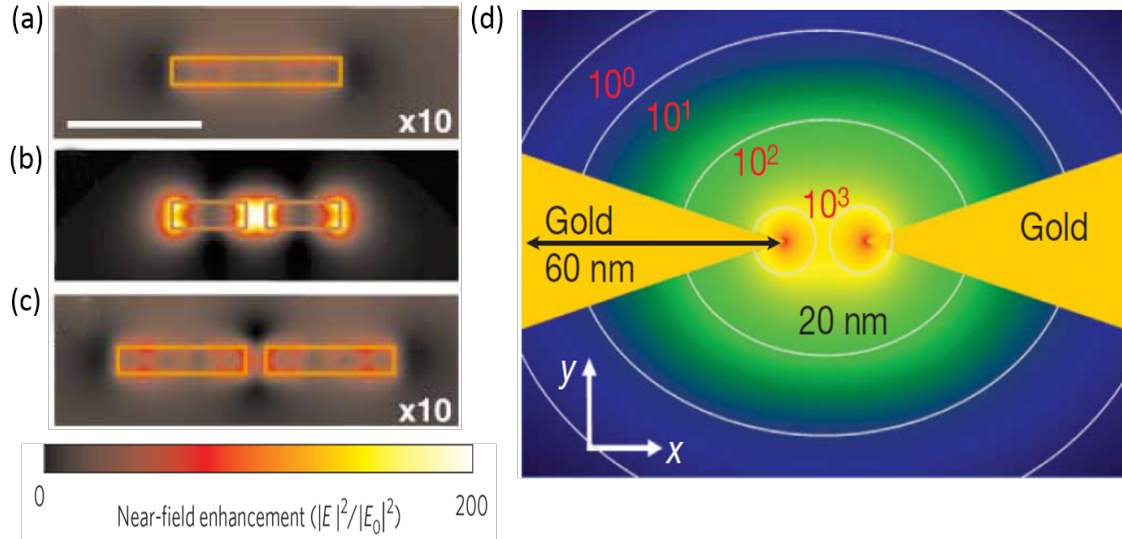
Figure 2.4 (a)-(c) Near-field intensity enhancement factor of gold structures on glass substrate, computed 10 nm above a stripe (250 × 40 nm), a resonant antenna (250 × 40 nm), and an off-resonant antenna (410 × 40 nm), respectively. The feed-gap width is 30 nm, and excitation wavelength is 830 nm; (d) Intensity field computation of bowtie antenna with 20 nm feed-gap. Reproduced from [24][25].

Strong plasmonic field concentration can be further improved by introducing a small gap in a metal structure, which is called a feed-gap [24][26]. Figure 2.4 a-c gives the intensity evolution of the strip structures without a feed-gap, with a feed-gap on-resonance, and with a feed-gap off-resonance, respectively. To satisfy the boundary condition that the normal field components must be continuous across the interface, the electric field in the dielectric gap will be enhanced by a ratio of $|\varepsilon_m/\varepsilon_d|$, where ε_m and ε_d is the optical constant of the metal and dielectric, respectively. Metals possesses a relatively large negative permittivity, so the ratio can be on the order of ten to a hundred. This feed-gap with a confined electric field is also referred to as a "hot spot". The geometry could be further modified to bowtie structures [27][28], mimicking a "lightning rod"

9

effect (Figure 2.4b). Oscillating free electrons at very high density are physically squeezed to a small volume near the sharp metal tip, resulting an extreme intensity enhancement with field ratios around 10^3 [29]. Bowtie antenna structures have widely been used as field concentrators for emission control [30], high efficiency nonlinear conversion[25], high Q deep-wavelength confinement [31], single molecule tracking [32] and reconfigurable nano-antennas [33].

Other geometries of plasmonic structures have also been designed to realize field confinement, such as an epsilon near zero mode [34][35], split-ring resonators [36]- [38] or hybrid mode [39]. Plasmonic resonances are not limited to metals, they can happen in non-metal materials such as highly doped semiconductors when carrier concentration is high enough to provide a negative permittivity [40]. Figure 2.5 gives a materials map with optical properties: the carrier concentration and carrier mobility. Lower carrier concentration and mobilities translate to higher material loss, which will be eventually dissipated as heat. The ideal plasmonic material should lie at the bottom left of the plot the with a nearly zero interband losses, which still remains elusive. These inevitable losses present one of the main challenges for plasmonic material and device development at high frequencies. Although loss-compensation approaches have been proposed, they make the system quite complicated and it is difficult to generate enough gain to fully compensate losses [41].
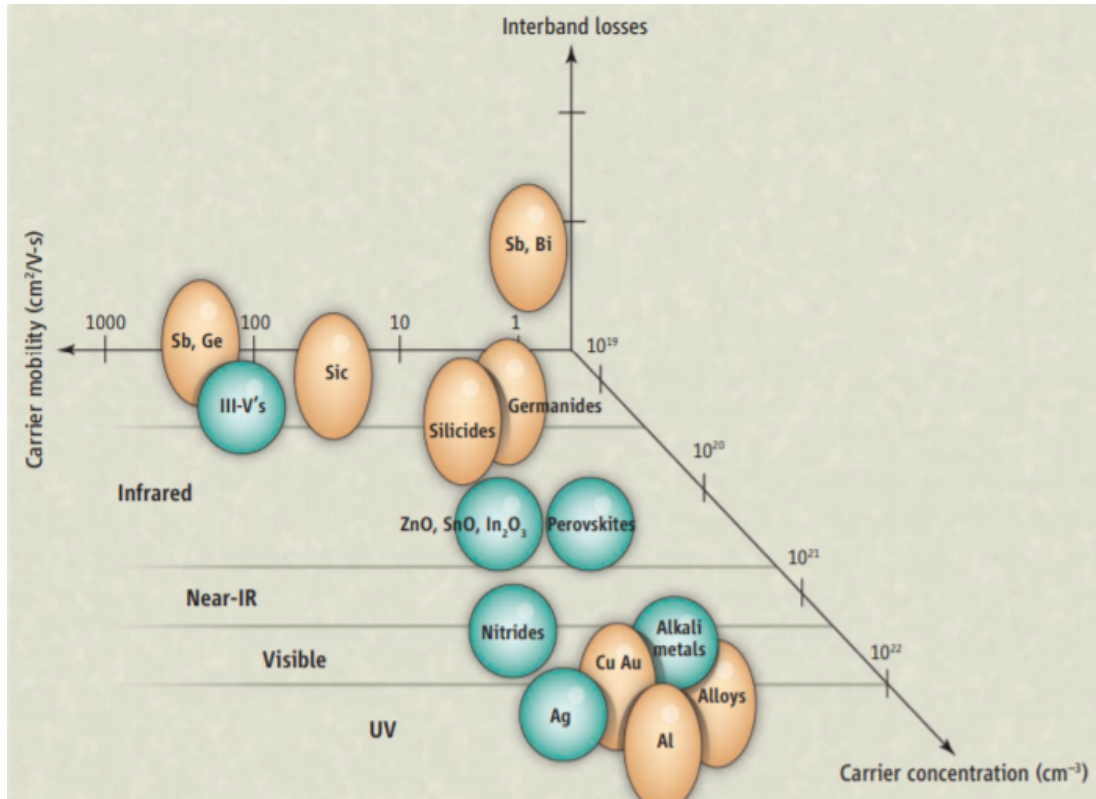
Figure 2.5 Metamaterial map for plasmonic applications, with interband losses, carrier mobility and carrier concentration plotted. Spherical bubbles represent materials with low interband losses, and elliptical bubbles represent those with larger interband losses in the corresponding part of the electromagnetic spectrum. [40]

2.1.2 All-Dielectric Nanostructures

One strategy to overcome the nonradiative loss of plasmonic systems is to use all-dielectric materials. High refractive index, subwavelength dielectric nanostructures possess Mie resonances which can take the place of plasmon excitations [42]. Mie scattering was first formalized at the beginning of 20th contrary when a German physicist Gustav Mie computed the scattering of electromagnetic wave by a homogeneous dielectric sphere and showed that the sharp absorption bands depended on the particle sizes, with results published in 1908 [43]. In 1946 by combining Mie scattering theory with Clausius-Mossotti effective medium theory (EMT), Leonard Lewin

systematically [44] predicted that the effective permittivity and effective permeability could be modified to be a negative value by the use of high index spherical particles. Recent investigations have shown that low loss electromagnetic resonaces covering all of the four quadrants in Figure 2.1 have been realized with all-dielectric metamaterials, including all-dielectric broadband perfect reflectors [45], negative and zero refractive index materials [46]-[48], magnetic mirrors [49][50]. The low loss of these materials allows for high quality factor resonances for biosensing and high spectral resolution imaging [51][52], as well as designing high efficiency ultrathin metalens systems formed intom a phased array [53][54].
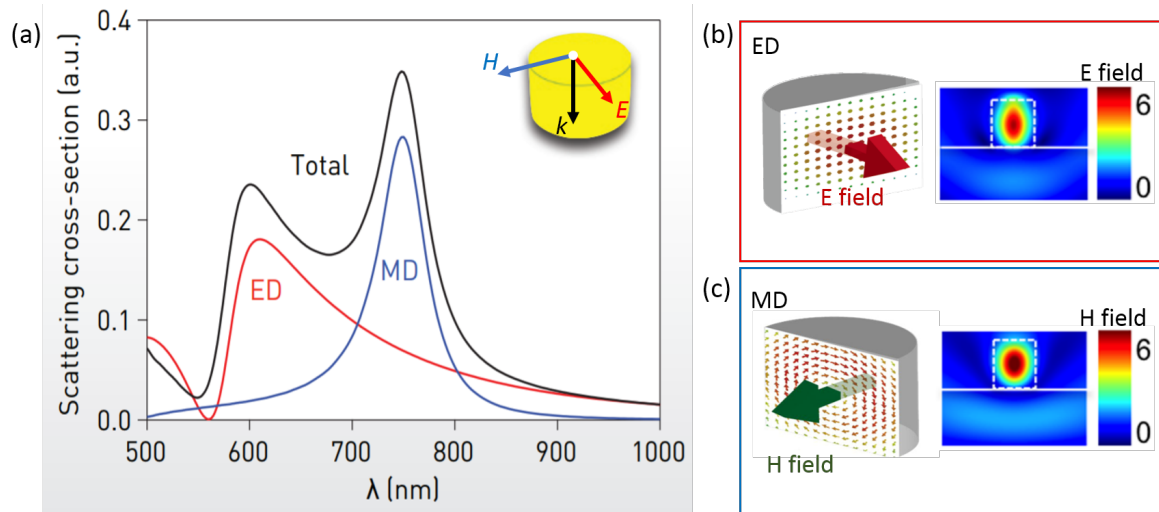
Figure 2.6 Scattering cross section of a subwavelength nanodisk at both ED and MD resonance positions (a), and the electric and magnetic field distribution inside the nanodisk cylinder for (b) ED and (c) MD, respectively [55].

In addition to the low-loss response, when working below the material band edge, there are other advantages to all-dielectric materials. To begin with, one single cylinder or post dielectric structure can support two fundamental Mie resonance modes, which are electric dipole (ED) and magnetic dipole (MD) resonance. The spectral positions of ED and MD are both affected by the

aspect ratio (AR) of the resonators. The ED resonance has oscillating electric field distribution between the structure boundaries, which makes the resonance more dependent on the in-plane diameter. The MD resonance leads to circulating electric field with resonance relying on both diameter and height. The lattice constant can also be controlled to change the coupling between neighbored unit cells and realize anisotropy in metamaterials [56]. Based on this, the spectrally resonant position could be tuned to any arbitrary frequency by changing the in-plane parameter as well as the height. The ED and MD resonances can be separated or overlapped, and separating the resonances helps to broaden the operational bandwidth [57].

Table 2.1 Refractive indices and absorption coefficients for high index dielectrics in visible near infrared and mid-infrared range.

Materials	@ 650nm		@ 1.4µm		@5µm	
	n	α (cm^{-1})	n	α (cm^{-1})	n	α (cm^{-1})
Si	3.9	3182	3.5	9e-8	3.4	5.1e-2
Ge	5.3	1.3e5	4.4	5.7e3	4.1	~
Te	4.35	4e5	4.72	3e4	4.9	~
GaAs	3.83	3.5e4	3.4	933.1	3.3	69.9
InAs	3.9	1.1e5	3.5	9.7e3	3.5	38.9
GaP	3.3	0	3.1	0	3.1	0
InP	3.3	5.9e4	3.2	401.5	3.1	30.2
AlSb	3.8	2.6e4	3.3	3.8e3	3.2	426.5
GaSb	4.9	1.8e5	3.8	1.1e4	3.7	348.8
TiO$_2$	2.4	2.1e-4	2.3	0	2.1	0.5

Platforms based on silicon are also compatible with silicon waveguides, and CMOS electronics. In addition, dielectric materials themselves are generally cheaper and more chemically stable compared to some plasmonic materials such as silver. This avoids additional coating procedures for passivation layers. In Table 2.1, refractive indices and absorption coefficients for high-index materials available in the visible and infrared are listed, among which silicon and germanium are widely used in near infrared and mid infrared [53] and TiO_2 is more widely used in visible wavelength due to its large bandgap [54].

In a dielectric resonator, the fundamental ED and MD resonances offer enhanced electric field both in plane and out of plane (Figure 2.6). Most of the light intensity is confined inside the resonator and it is easy to obtain an enhancement ratio around 10 [58]. Like plasmonic metamaterials, coupled all-dielectric resonators could also create interacting hotspots for various applications by introducing a narrow gap between two nanodimers (Figure 2.7a). Compared to one dielectric resonator, coupled resonators can obtain higher field confinement efficiency and unique functionalities – magnetic hotspot specifically. In figure 2.7b, the finite-difference time-domain (FDTD) simulations and near-field scanning optical microscope (NSOM) image of two coupled silicon nanodimers reveals that the electric and magnetic field enhancement with a ratio of 6 could be reached experimentally at ED and MD resonance frequencies.
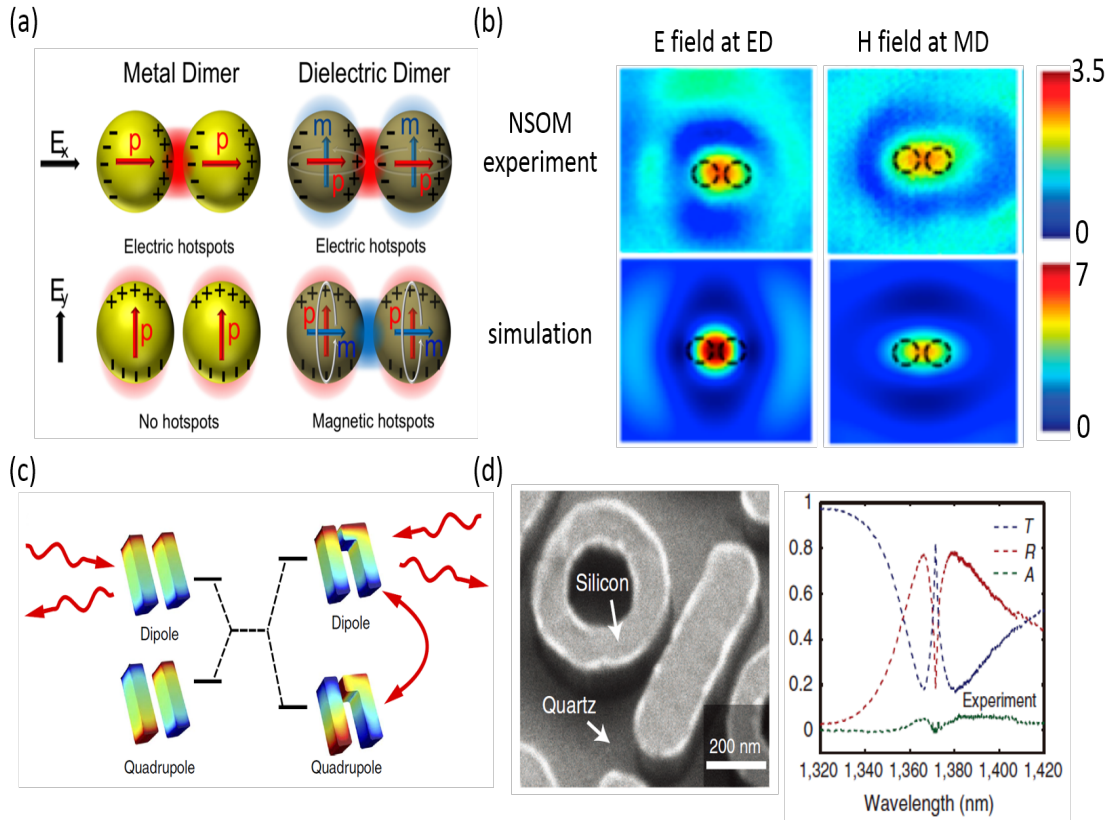
Figure 2.7 All-dielectric coupled metamaterials. (a) Schematics for electric and magnetic hotspots generated by silicon nanodimers; (b) FDTD simulation and NSOM measurement of the electric and magnetic field profile at ED and MD resonance positions, respectively. This paper reports the first experimental demonstration of electric and magnetic hotspots generated from isolated nanodimers; (c) Schematic of Fano resonance between the electric dipolar and quadrupolar modes of two silicon rods due to symmetry breaking; (d) An analogue of electromagnetically induced transparency realized by Fano resonance in all-dielectric metamaterials. Figure reproduced from [52][58][60].

Coupled all-dielectric metamaterials can also lead to metamaterials with a high-quality factor by exploiting Fano resonances. A Fano resonance happens when interference between a background continuum and a resonant scattering process produces asymmetric line-shape. It can form a sharp feature in the absorption or transmission spectrum when a bright mode and a dark mode spectrally overlap and interact with each other [52] (Figure 2.7c). This interaction can

generate nanoscale hotspots, which could be used to enhance the nonlinear conversion efficiency [59]. The Fano resonance is also quite spectrally sensitive to the surrounding medium refractive index change, which could be applied as chemical sensors [60].

The field confinement capability of all-dielectric resonator is inferior to that of plasmonic structures, but a significant advantage is the lack of loss. With single or coupled resonators, the electric field hotspots can be selectively located inside or around the structures, offering a convenient route to integrate with other functional platforms, for example quantum dots for spontaneous emission control applications, active materials for dynamic control and optical modulation, and ultrathin materials for enhanced absorption [51][62].

2.3 Reconfigurable Metamaterials

By proper selection of the construction materials and design of the structure geometry, metamaterials can exhibit customizable optical properties, accompanied with features like localized enhanced electrical fields, mode coupling, and phase gradients. However, most metamaterials are passive, which means the properties can not be modified once they are made through all of the complicated nanofabrication processes. Reconfigurable metamaterials (metadevices) have been proposed to solve this problem, aiming to realize dynamic control of the device performance, such as light propagation direction, intensity, phase and polarizations [63][64]. Reconfigurable metamaterials typically consist of metal or dielectric nanostructures to support spectral resonances, and active functional medium with tunable optical parameters. Examples of plasmonic resonant structures assisted metadevices have been demonstrate with carrier injection into semiconductors, metal oxides, or 2D materials [65]-[76], molecule orientation changes in liquid crystals [77]-[80], thermal and electromechanical metamaterials[81][82]. Figure 2.8 summarizes some featured works with these approaches such as electrical method, micro-electro-mechanical systems (MEMS), temperature change, optically active carrier doping or chemical composition, respectively [83]-[87].
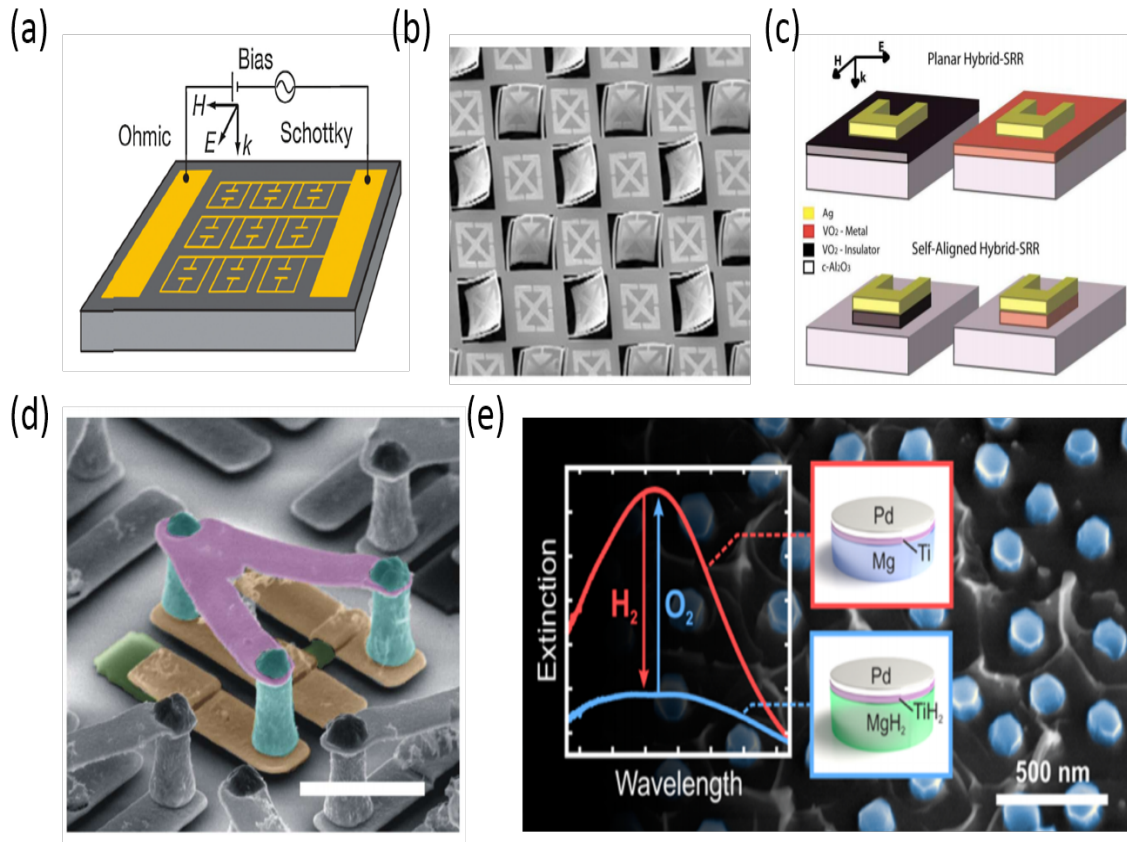
Figure 2.8 Reconfigurable metamaterials controlled with (a) electrical method, (b) mechanical method, (c) thermal approach, (d) optical pump and probe, and (e) chemical composition change. Reproduced from [83]-[87].

Many researchers within the metamaterial community have also recently turned to active all-dielectric metasurfaces for the purposes of switching, spatial light modulation, and creating reconfigurable optical elements [88][89]. There have been several approaches to modulating optical properties of dielectric metasurfaces, but all contain serious drawbacks similar with plasmonic structures. Fabricating Mie resonators on stretchable substrates like PDMS to change the lattice constant is always restricted by the yield of the stretchable film, which is typically less than 10% for reversible control [90]; LC molecules can be orientated with temperature change, UV irradiation

17

or external voltage bias. But metasurfaces integrated with liquid crystal are bulky (~150μm) due to the usage of the rubbing layer and therefore not power efficient [91]-[95], and the relaxation time is in the millisecond range. Modulation of carrier concentration via injection [96]-[102], however, can achieve modulation depths of around 40%, but requires intense pump or very high temperature (>573K) [103]. The response speeds are also limited by the carrier lifetime. Meanwhile some film preparation protocols have to rely on molecular beam epitaxy (MBE) growth, and are far from being commercially ready. Microfluid and MEMS systems have been reported for tunable color displays and metasurface lenses, but are hardly compatible with other systems [104][105].

Phase-change materials such as chalcogenide glass (GST) (non-volatile) and VO_2 (volatile) have been used for decades in memory storage [106][107], and dynamic optical elements such as tunable absorbers and polarizers [108]-[119]. Vanadium dioxide (VO_2) is particularly interesting as it has a reversible insulator to metal phase transition (PT) at near room temperatures (~340K), which is critical for realizing low power devices. More information about phase change materials will be given in chapter 3. Recently phase change media have also been introduced to the all-dielectric tunable metasurface community, yielding large modulation depths with PT triggered via temperature [120]-[123].

2.5.1 Challenges for Reconfigurable Metamaterials

Although numerous reconfigurable metamaterials have been demonstrated, obtaining active control of light remains an elusive and ambitious task, especially in the shorter wavelength region. The major limitations come from (1) the availability of active media which allow the electromagnetic parameters to be tuned dramatically with acceptable external stimuli; (2) the difficulty in integrating metamaterials with small active volumes to enhance the response speed and decrease average power consumption.

Phase change materials are promising candidates for reconfigurable metamaterials in the near infrared wavelength considering its large dielectric function change across the PT, which could be implemented to overcome the first limitation. The majority of previously demonstrated reconfigurable metamaterials, including the PCM-based metamaterials, have employed continuous films that can be readily incorporated into structured metal resonators, behaving as surrounding medium, space layer, or substrate. However, when switched thermally or electrically the large mass of continuous films necessitates large switching power per bit. At the same time, it limits the switching speed as this thermal energy must then be dissipated to fully recover the device. Based on the above considerations, decreasing the active materials volume or mass is necessary to improve the overall performances of reconfigurable metamaterials, especially in applications which require ultrafast modulation.

2.5.2 Decreasing the Thermal Mass of VO_2 Phase Change Materials

For VO_2 phase change materials, decreasing the thermal mass to microscale or nanoscale structures could realize the following benefits. First of all, VO_2 in the semiconducting phase has a band gap of approximately 0.6eV [124]. There is a non-negligible natural absorption of VO_2 even in the semiconducting state when working in the near infrared region. Decreasing the VO_2 volume could reduce the on-state loss, therefore increasing the on/off ratio (modulation depth) for light modulators. Secondly, replacing the continuous film with isolated VO_2 crystal grains means that the overall switching energy will be dramatically lowered. In addition, with the help of the metamaterial field concentrator the absorption in each particle corresponds precisely to the incident light intensity. Enhanced absorption decreases the switching threshold and make more energy efficient devices. And this becomes more and more important in the future for on-chip optical circuits as the integration will be partly determined by the power consumption and dissipation.

Lower energy also goes with fast recovery from off state to on state. Finally, it has been proved that VO$_2$ nanoparticle arrays show a broader switching energy distribution due to the size effect. Utilizing these nanocrystals instead of continuous film in metamaterials is beneficial to broaden the dynamic range and achieve multi-level or multi-state storage and modification.

CHAPTER 3 PHASE CHANGE MATERIALS

3.1 Optical Phase Change Materials and Applications

A phase change material (PCM) is generally a substance that can exhibit transformation from one crystal structure to another in response to external excitation, for example temperature change, intense electric field, stress or laser excitations. In addition to PTs involving different atomic configurations, PCMs also undergo electronic or changes of spin configurations, allowing for controllable modification of materials' optical, electrical, and/or magnetic properties. During the PT, the free energy in the system stays continuous, while the thermodynamic quantities such as volume and heat capacity can be discontinuous. Phase-change materials can be classified as first-order or second-order PCMs based on which derivative of the free energy shows discontinuous change.
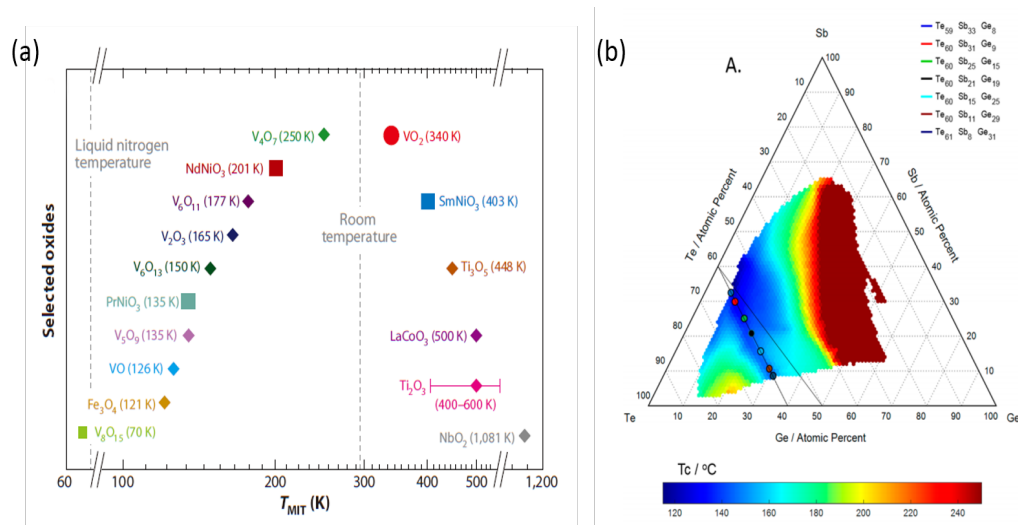
Figure 3.1 Optical phase change material PT temperature mapping. (a) The insulator-metal transition temperatures of some transition metal oxide bulk crystals; (b) Amorphous to crystal transition temperature for Te-Sb-Ge based alloys with different composition percentage. Reproduced from [125][126]

Transition metal oxide (TMO) and chalcogen-based alloys [127] constitute two of the most fascinating classes of inorganic optical PCMs. Figure 3.1 shows the thermal PT threshold for these two groups. Materials like VO_2 shows volatile property, the initial property recovers once the stimuli get removed. Applications for dynamic or real-time control could benefit from this property, including smart windows [128][129], optical switches [130][131], sensors and bolometers [132]-[134]. On the other hand, chalcogen-based alloys are generally non-volatile and melting is required to return to the off state, and are for that reason widely used in data storage [135][136].

3.2 Vanadium Dioxide Phase Transition

Vanadium dioxide (VO_2) is a first-order phase change material, which belongs to the transition metal oxide family. Several crystal phases have been reported namely M1, M2, T and R. Among these phases, M2 and T phase can be stabilized by applying small uniaxial stress on the basis of The M1 therefore they are interpreted as alternate phases of pure VO_2 [137][138], which will not be discussed in this dissertation. The M1 phase has been the most attractive because of the semiconductor-to-metal PT around 340 kelvin (K), which is close to room temperature. Below this critical temperature (T_c), VO_2 has a monoclinic lattice structure (M1) and exhibits semiconducting property with moderate resistivity, while above this threshold vanadium atoms move and form rutile crystal structure (R) and the material exhibits metallic property with low resistivity (Figure 3.2a) [139][140]. This VO_2 PT is both an electronic and structural transition, with the band structures of semiconducting and metallic states illustrated in Figure 3.2b [141]. The phenomenal range of electric and optical properties caused by PT of VO_2 is equally noteworthy, especially in the infrared regime. The relative change measured in the resistivity for a polycrystalline film can be up to four orders of magnitude (Figure 3.2c). Figure 3.2d shows the measured optical dielectric constants of 60nm radio-frequency (RF) sputtered VO_2 in the semiconducting and metallic states

in near infrared. High contrasts in both real and imaginary part of VO_2 permittivity are observed above 800nm wavelength, which makes VO_2 a potential candidate for applications in optical communication [142]-[145], memory devices [106][107], thermal management [146], gas sensors [132]-[134] as well as field-effect transistors [147][148].
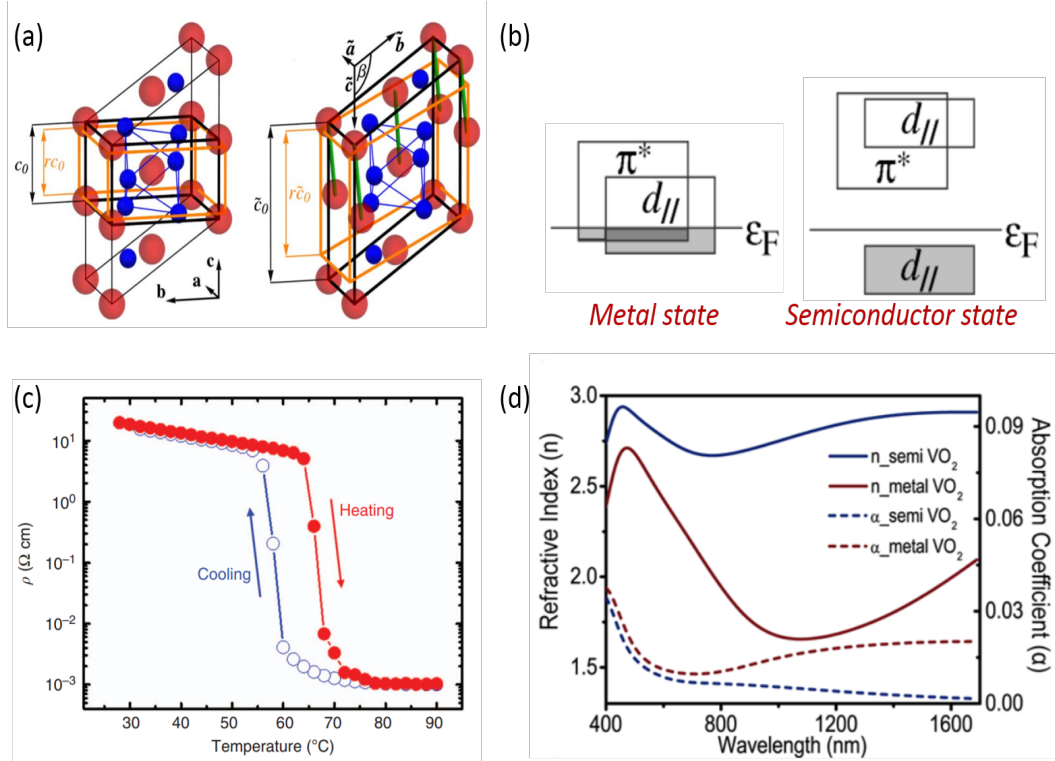
Figure 3.2 VO_2 properties. (a) Schematics of high temperature rutile and low temperature monoclinic lattice structure of VO_2. Large red spheres: V atoms; Small blue spheres: O atoms. (b) VO_2 band structures in metallic and semiconducting state. (c) Temperature-dependent resistivity of 30nm VO_2 film grown on sapphire substrate. (c) Measured refractive index and absorption coefficient of RF sputtered VO_2 film on silicon substrate. Reproduced from [139]-[141].

The vanadium dioxide semiconductor-to-metal phase change is a first order PT process. Similar to other first order phase changes, a 1.7% volume and density change are observed for VO_2 because of the atom rearrangement (Table 3.1). The thermal properties like conductivity and heat

23

capacity change substantially due to the electron thermal conductivity contribution, indicated from the Wiedemann–Franz law [149]. All of the above property changes make it possible to directly and indirectly identify and study this process, for example using four-point probe to measure film conductivity, using optical hysteresis setup to measure the extinction coefficient of the film, using high resolution electron microscope (HREM) or tunneling electron microscopy (TEM) to indirectly monitor and trace the atom movement [150], or referring to Raman spectroscopy [151], X-ray diffraction (XRD) to obtain more information about the lattice (Figure 3.3) [152][153].

Table 3.1 VO_2 properties above and below the semiconductor-to-metal PT

Property	Below T_c	Above T_c	Change	References
Lattice Structure	Monoclinic	Rutile		[124][154]
Density	4.57 g/cm^3	4.65 g/cm^3	1.7%	[154]
Thermal Conductivity	3.5 W/(m K)	6.0 W/(m K)	71.4%	[155]
Heat Capacity	0.656 J/(g K)	0.78 J/(g K)	18.9%	[156]

Thermal heating is the most accessible approach and nanosecond response time has been demonstrated in hybrid silicon-VO_2 electro-optical modulator [157]. Apart from thermal method, VO_2 semiconductor-to-metal PT can also be triggered via strain, high electric field or ultrafast laser. Among those strain is mostly used in VO_2 single crystals, which is not a focus of this thesis. Electric field switching has long time been a goal for researchers however it is quite challenging to isolate the field effect from Joule heating effect as the field needed is also nearly equal to the breakdown voltage. No clear evidence of pure electric field-induced PT of VO_2 has been reported so far, to the best of current knowledge. Ultrafast laser induced PT has been attracting a lot of attention recently since it can be used to study the PT dynamics and potentially resolve the long-lasting debate between Peierls model (structural transition mechanism) and Mott-Hubbard (electronic transition

mechanism). Previous studies have shown that these two phenomena can be separated based on the time range [158]. The structure transition typically has a triggering time of a few picoseconds and a recovering time of hundreds picoseconds or nanoseconds, while the electronic transition can happen within 60fs. Semiconductor-to-metal transition occurs under femtosecond laser fluence with VO_2 staying in monoclinic lattice state, which can dramatically decrease the switching time as the structural transition is eliminated.
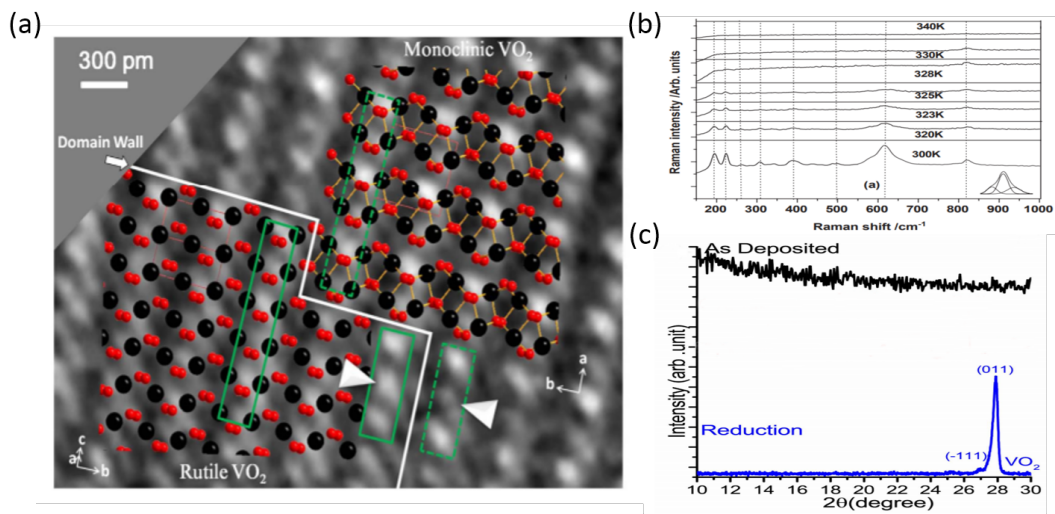
Figure 3.3 Other PT characterization methods for VO_2. (a) Smoothed high resolution TEM image of monoclinic/rutile domain walls. Insets show two-phase color atom model diagrams. The red spheres and black spheres represent O and V atoms, respectively; (b) Raman spectra of VO_2 thin film at different temperatures during the heating process. Vertical dotted lines show the positions of the major Raman lines of VO_2; (c) XRD patterns of as-grown film and monoclinic VO_2 M1 phase. Reproduced from [150][151][159].

The VO_2 PT threshold is also modifiable with applied strain or doping. Low valence dopant like Al^{3+}, Cr^{3+} shifts the T_c up, while high valence dopant, mostly used W^{6+} and Mo^{6+}, shifts the T_c down even to room temperature, depending on the doping level. This ability makes VO_2 a strong

PCM candidate for applications in daily life. Drawbacks are that the dielectric constant contrast and switching hysteresis width are sacrificed, which may need thicker VO_2 film to compensate.

3.3 Influence of Fabrication and Size Effects

In circumstances where we do not study the ultrafast PT phenomenon, VO_2 PT often exhibits lattice structure change. Therefore, different VO_2 polycrystalline grain size and boundaries caused by the film preparation affect the overall PT properties, such as switching threshold T_c, hysteresis width and switching contrast. The VO_2 growing conditions have been investigated for decades, covering factors such as deposition methods, substrate lattice, post annealing conditions for example annealing temperature, time and oxygen flow rate.
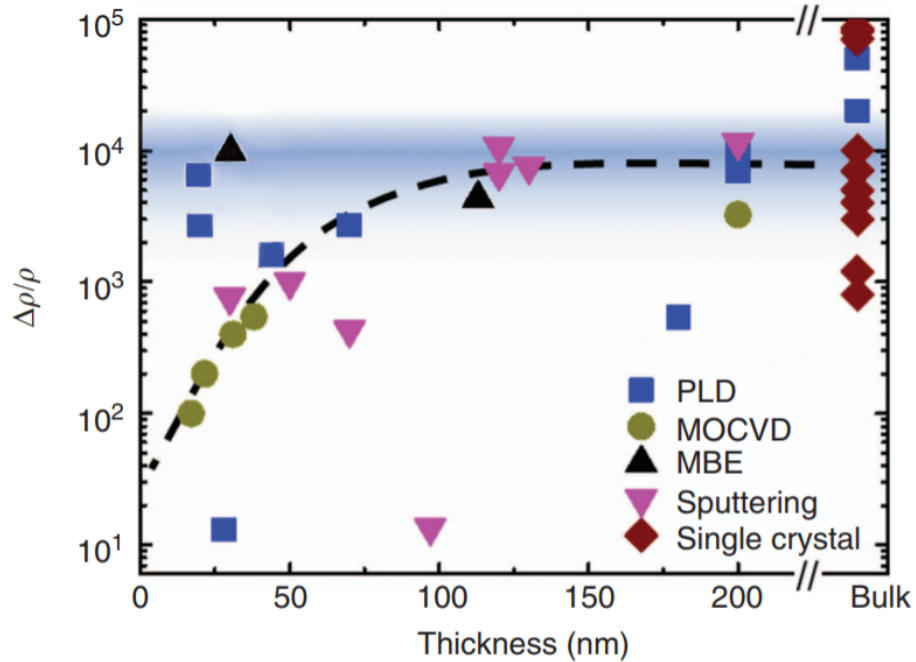
Figure 3.4 Benchmark of VO_2 thin films with resistivity ratio $\Delta\rho/\rho = (\rho_{50\,°C} - \rho_{80°C})/\rho_{80°C}$ for VO_2 across the semiconductor to metal transition. Here all the films are grown on Al_2O_3 substrate for direct comparison. Reproduced from [140].

From previous work [140], generally pulsed laser deposition (PLD) and metal-organic chemical vapor deposition (MOCVD) can produce ultrathin VO_2 film down to about 10nm (Figure 3.4). Pulsed laser deposition (PLD) comparably tends to give higher switching contrast due to the high-energy atoms and ions ablated by the KrF_2 excimer laser from the vanadium or VO_2 target. Sputtering is a more commonly used approach considering the easier deposition condition, and usually is used for thicker VO_2 film; it usually produces the densest films and smallest grain sizes. In addition, atomic layer deposition (ALD) of VO_2 has also been well developed by the Naval Research Laboratory with good uniformity and switching contrasts [160][161].

Among the three physical vapor deposition (PVD) methods - PLD, e-beam evaporation and RF sputtering - the surface energy and specially dewetting, have significant influences on the morphological evolution of the VO_2 thin film [162], with atomic force microscope (AFM) images shown in Figure 3.5. The corresponding optical hysteresis trend is depicted in Figure 3.6, considering factors such as substrate and annealing time as well.
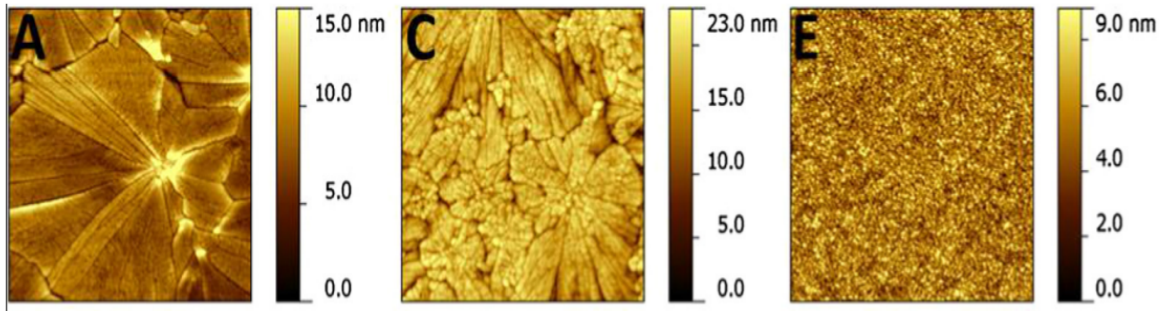
Figure 3.5 AFM morphology images of VO_2 film grown by (a) PLD, (b) ebeam deposition, (c) RF sputtering method. All images are 2 μm × 2 μm. Figure reproduced from ref [162].
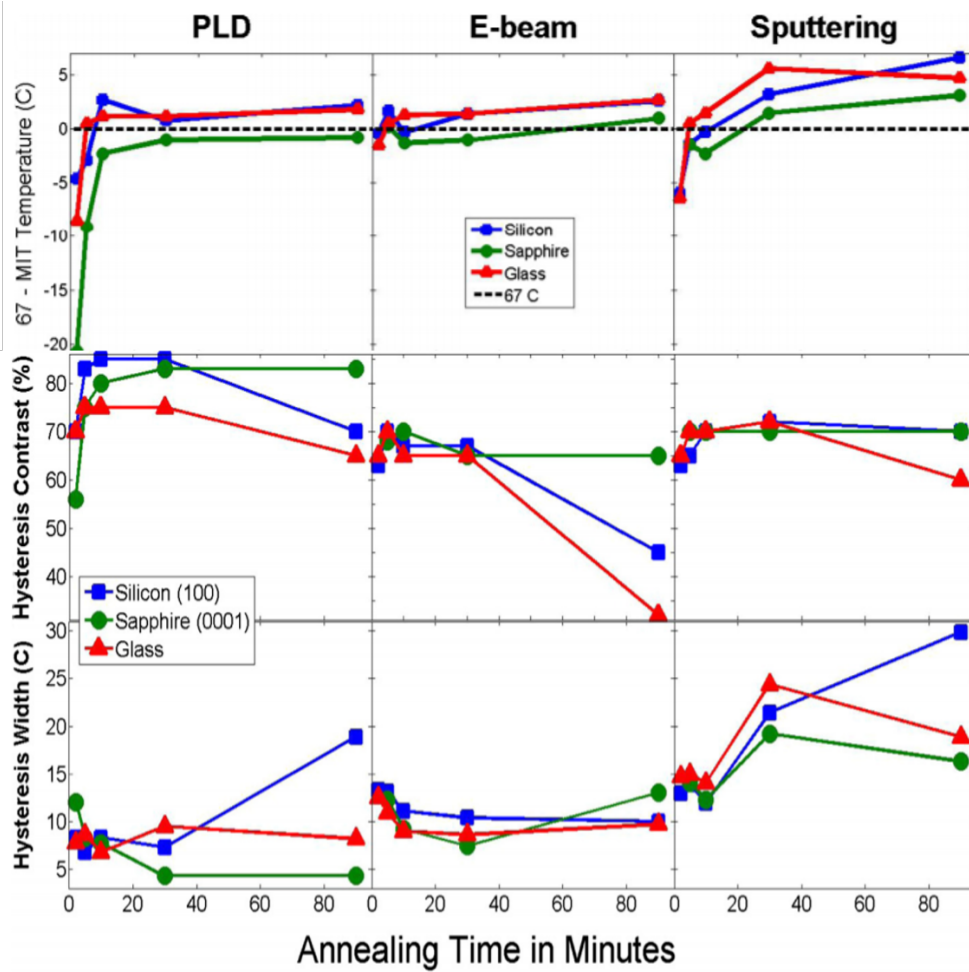
Figure 3.6 A complete comparison about the PT properties (threshold, switching contrast, and hysteresis width from top to bottom) which is dependent on deposition method, substrate, and post annealing time. Here the light source is 1550nm and samples are annealed at 450 °C in 250 mTorr O_2 environment [162].

The VO_2 films deposited by PLD also have very high density due to the high energy plumes that the laser ablates from the target surface . As a result, PLD film has higher hysteresis switching contrast and narrower width, which is clearly shown in Figure 3.6. RF sputtering method gives wider hysteresis, which indicates that the crystal grains as well as the switching temperatures for individual grains are more broadly distributed. We can also tell that sapphire substrate gives the best films for all of the three approaches considering the epitaxial growth beneficial from the lattice

28

match. With a better lattice matching substrate such as TiO_2 (001) (lattice mismatch: 0.86%), VO_2 film with 10^3 relative resistivity change has been reported with 10-15nm thickness [163]. Longer annealing time also plays a big role in modifying the hysteresis contrast and width for the PVD methods, attributed to the accumulating dewetting phenomenon.
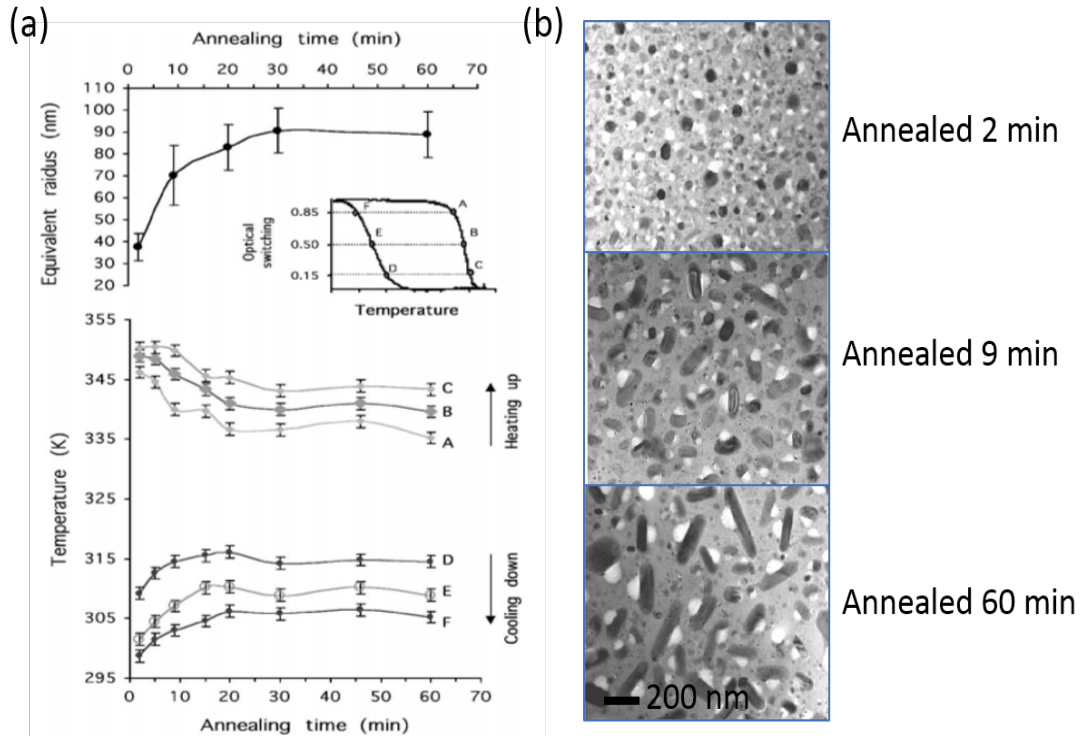
Figure 3.7 Size effect of the VO_2 nanoparticles (a) VO_2 precipitate size related to annealing time (top) and the corresponding optical transmission switching at 1.5μm as a function of the annealing time (bottom). The inset shows a typical hysteresis loop, marked with indicator points (A, B, C, D, E, F) used to quantify the switching; (b) TEM images of the VO_2 precipitate in SiO_2 for selected annealing times. The samples were prepared by implanting SiO_2 with 1.53×10^{17} V ions/cm2 at 150 keV and 3.0×10^{17} O ions/cm^2 at 55 keV and then annealing in argon at 1000 °C. Figure reproduced from [164].

Although there have been important advances in understanding the PT of VO_2 through related film stoichiometry, grain evolution and other morphological faults, it would not be complete

29

without studying the role of reduced dimensionality. Compared to continuous films, it has been proved that VO_2 nanoparticles with smaller equivalent radius have PT starting at lower temperatures and completely finishing at higher temperature, as a result, exhibiting broader hysteresis [164]. This phenomenon is referred as the size effect of VO_2 (Figure 3.7). Later surface-enhanced Raman scattering and optical response of ordered VO_2 nanoparticle arrays were studied, providing critical insights into statistical processes occurring in materials at the nanoscale [165][166]. These properties also become more and more relevant as VO_2 approaches nanotechnology applications, leading to energy efficient nanodevices as well as potential usage in neuromorphic computing systems [167].

CHAPTER 4 NEAR INFRARED REFLECTION MODULATOR WITH PLASMONIC METAMATERIALS

4.1 Introduction

In this chapter, we present a reconfigurable metamaterial that integrates VO_2 nanocrystals with plasmonic metamaterials. By designing the unit cells so that each nanocrystal is in the feed-gap of a bow-tie antenna, we achieve strong field concentration within the VO_2 nanocrystals. This allows the metadevice to be more sensitive to the optical properties of the VO_2 while also utilizing a small thermal mass for reduced switching power and time. In addition, the metallic unit cells serve as the heating element minimizing the volume that must be heated and improving integration. This results in an integrated device with a modulation depth of 33% within the telecommunications band and a 1.27ms recovery time [108].

4.2 Design Methodology and Simulation Results
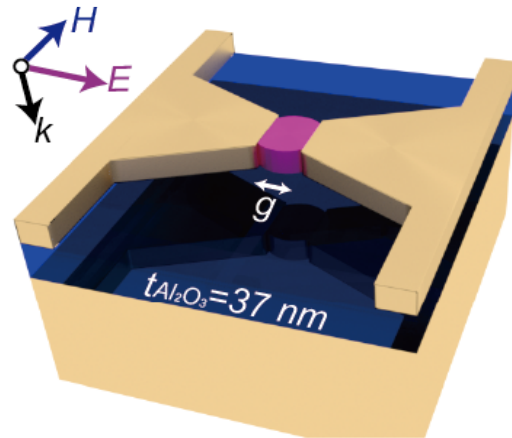
Figure 4.1 Schematic of the MPA structure with unit cell dimensions: lattice pitch p_x=264nm, p_y=300nm, wire width: w=100nm, and gap width: g=34 nm.

A typical multilayer (metal-dielectric-metal) metamaterials perfect absorber (MPA) is used in this design. For the top structured layer, we use bowtie shape concentrator to support the electrical dipole resonance as well as greatly enhanced electrical field in the feed-gap, while the coupling between the top bowtie structure and the metal backplane forms the magnetic dipole (Figure 4.1). When these two resonances are spectrally overlapped, the destructive interference of the reflection will lead to perfect absorption. The power loss density is dictated with the imaginary part of the local materials' permittivity multiplied by the square of the electrical field. When VO_2 phase change materials are embedded in the bowtie feed-gap, from the FDTD simulation results in Figure 4.2a, b, we can see the majority power loss is concentrated in the VO_2 patch. This is the key to amplify the optical parameter change in the VO_2.
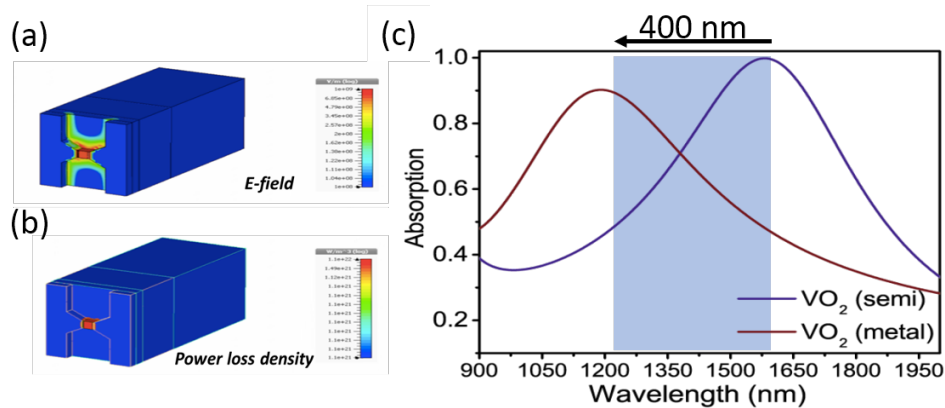
Figure 4.2 Simulation results. (a) The electric field and (b) power loss density distribution of the MPA at the metamaterials resonance frequency with the VO_2 is in semiconducting phase; (c) simulated absorption spectra of the MPA with VO_2 permittivity obtained with semiconducting and metallic state VO_2.

To verify the idea and understand the evolution of the optical properties with temperature, we performed FDTD simulations with VO_2 optical properties acquired using ellipsometry on 60nm thick films (Figure A. 1). The absorption spectrum showed nearly unity absorption at 1590 nm and kept constant below 55°C, while blueshifts to approximately 1190nm at 70°C and finishes the

transition by 75°C. The wavelength shift reached up to 400nm, meanwhile at the resonance positions below and above the VO_2 PTs, the calculated modulation depth is around 50%, which is a very large value compared to other near infrared free space modulator devices.

4.3 Fabrication of The Active Metamaterials

The metadevice is based on the perfect absorber (MPA) architecture with each unit cell consisting of a gold bow-tie antenna with a small VO_2 patch placed in its feed-gap. This layer is separated from a thick gold backplane by a thin Al_2O_3 dielectric spacer layer. Fabrication began with thermal deposition of 5nm/100nm of Chromium/gold (Cr/Au) on fused silica to form the backplane (see the material selection in A.3). This was followed by ALD of 37nm of Al_2O_3 to form a transparent dielectric spacer layer. And then three electron beam lithography (EBL) processes are used to define the following structures.

Alignment markers with dimensions 0.3μm × 10μm (W × L) and external electrodes (200μm × 200μm for local heating purpose) were first fabricated on the Al_2O_3 film by EBL and 5nm/150nm Cr/Au deposition (a, b). And then VO_2 patterns ($120 \times 120 \times 37nm^3$) were then defined on the Al_2O_3 film by electron beam lithography on liftoff photoresist, which is 50nm PMMA 495 A2 plus 70nm 950 A2 stack (Figure 4.3c). This liftoff photoresist is very critical for defining tiny nanostructures with nearly isotropic deposition. Here the VO_2 patch was also designed larger than the feed-gap size to guarantee perfect alignment with the bowtie array, as well as to avoid PMMA gap closure in the deposition step. After development using MIBK:IPA=1:3 developer and 6s O_2 descum, the $VO_{1.7}$ was sputtered using a two-inch vanadium metal source in a 6mTorr Ar and O_2 environment, with flow rate of 20sccm :1sccm (standard cubic centimeter per minute), and a deposition rate of 1.2Å/s. A standard lift-off procedure was followed and then a post annealing was

performed for 5min at 450°C in 250mTorr O_2 environment with flow rate around 17sccm to crystallize the VO_2.
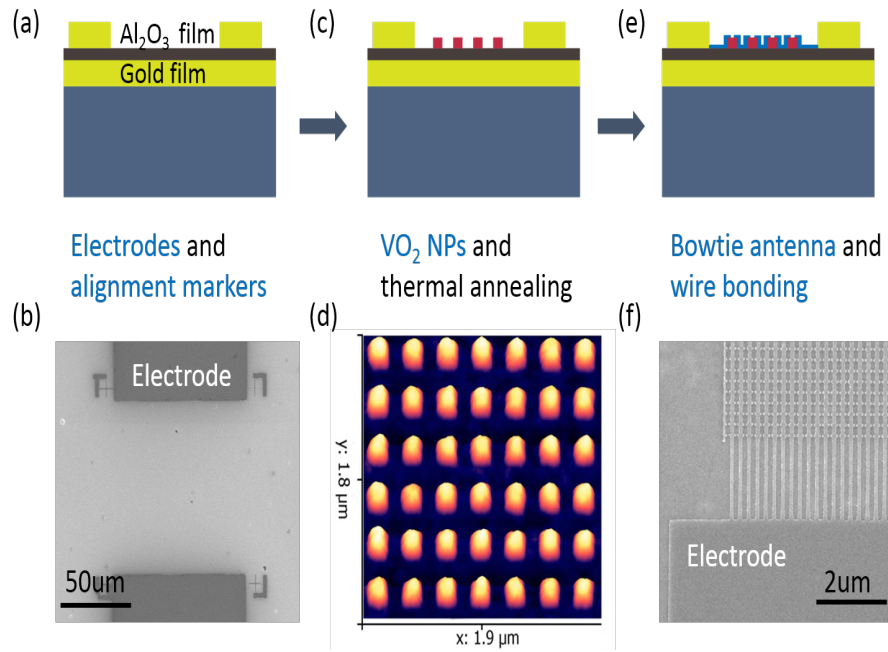
Figure 4.3 VO_2 based MPA active metamaterials structure defining processes. (a)(b) external electrodes and alignment markers patterning and scanning electron microscope (SEM) image; (c)(d) VO_2 nanoparticles defining and AFM image of the nanocrystals after liftoff and post annealing process; The AFM image has a height scale of 0-37nm. (e)(f) Top bowtie antenna overlapping and SEM image of the final device, showing the electrodes and array.
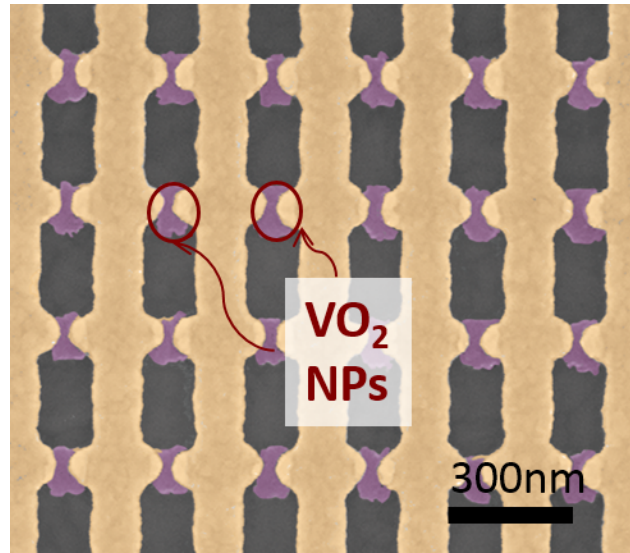
Figure 4.4 False color SEM image of the MPA active metamaterial array. The VO_2 nanocrystals are colored purple while the connected bowtie antenna is colored in yellow.

After the VO_2 patterning and crystal process, gold bow-tie antennas with 34nm wide feed-gaps were then overlaid onto the VO_2 nanocrystals using electron beam lithography, thermal deposition and lift-off (Figure 4.3e, f). The thickness was 3nm/30nm Cr/Au. The smallest possible gap size is preferred as it increases the capacitance in the semiconducting state, red shifting the resonance and resulting in a larger wavelength change upon switching. More details about the gap size dependence can be found in Appendix A.2. These antennas were connected by bus bars which were connected to large external gold electrodes so that the antennas can serve as integrated heating elements. A zoomed SEM image of the final device is given in Figure 4.4, with false color for better identification (purple: VO_2 nanoparticles; yellow: bowtie antenna). From the SEM we can tell all the VO_2 nanocrystals are all perfectly aligned in the feed-gap of the bowtie antenna.

4.4 Device Characterizations

After the device fabrication, the optical measurements were carried out using a super-continuum light source (Fianium) and the reflected signal from the sample was analyzed using a grating spectrometer with an InGaAs detector (Horiba iHR320). A 50× infrared objective was used to focus the light into the metamaterial array. Since the transmission was totally blocked by the 100nm gold backplane, so absorption of the metamaterials could be calculated with $A = 1 - R$.

4.4.1 Temperature Dependence

In order to characterize the modulation depth, the metadevice was first mounted on a temperature-controlled stage. A white-light supercontinuum source was incident onto the metadevice using a 50× objective, with the polarization perpendicular to the bus wires. The MPA absorption curve is shown in a. The measured resonant position shifts from 1590nm to 1230nm as the stage temperature increases from 21°C to 87 °C, with the resonance and absorption magnitude evolution shown in Figure 4.5b. This results in a figure of merit of FOM = $\Delta\lambda/\lambda$FWHM = 82%. The reversible modulation depth (defined as $h(\lambda) = |A_{max}(\lambda) - A_{min}(\lambda)|$) was experimentally measured to be 27% and 33% at 1232nm and 1588nm, respectively. These are among the highest values measured in free space within this wavelength regime, to the best of our knowledge. It should also be noted that compared to VO$_2$-film based metadevices, we observe a change in the switching temperature range resulting from the small size of the VO$_2$ nanocrystals. The modulation starts earlier at about 40.3°C and finishes at 86°C, which provides greater dynamic range for grey-scale control. The PT range was simulated to be 20°C while the experimental result in Figure 4.5a has a range of over 37°C. The wider transition width for the nanoparticles is consistent with larger inhomogeneity in grain size. It is also consistent with a broadening of the resonance due to inhomogeneity in the fabricated bowtie antennas.

36
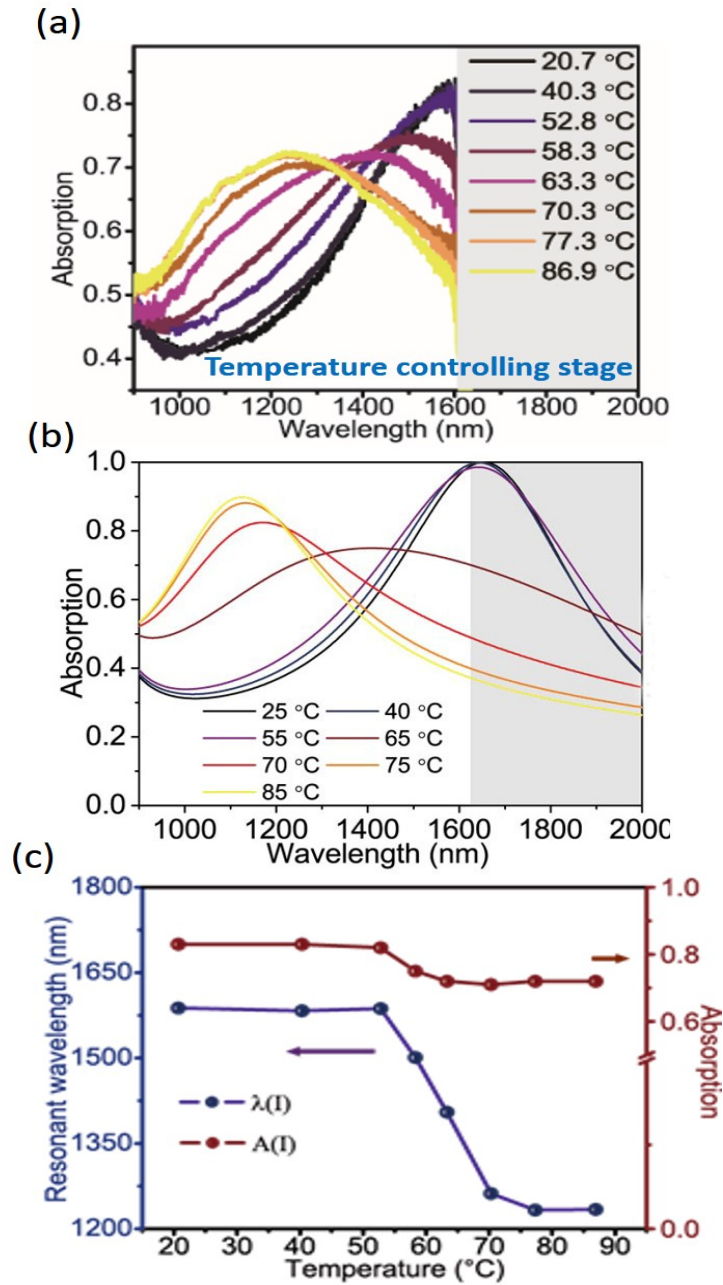
Figure 4.5 Temperature dependence of the MPA active metamaterials (a) Measured absorption spectra of the metadevice at different temperatures; (b) Simulated absorption spectra with VO_2 permittivity obtained at different temperatures; (c) Resonance wavelength (left axis blue) and absorption magnitude (right axis red) evolution with the temperature change in the device.

Overall the performance of the metadevice agrees well with full-wave finite-difference time-domain (FDTD) simulations shown in Figure 4.5c. In these simulations the VO_2 properties were extracted from the experimentally measured optical properties shown in Figure 3.2d. Based on the simulated absorption spectrum, when the VO_2- based metadevice is in the semiconducting state (25°C), the device exhibits almost unity absorption (99.7%) at a resonant frequency of 1590nm. At an intermediate state of 65°C the resonance shifts to approximately 1380nm with a peak absorption of 73%. The resonance further shifts to 1190nm as the VO_2 becomes metallic (85°C) with a peak absorption of 90%. The simulated structure has a slightly larger tuning range (400nm) and modulation depth (48% and 51% at 1590nm and 1190nm, respectively). The deviation between the simulated and experimental modulation depth can be attributed to several factors. The ellipsometry data used in the FDTD simulations were acquired from a 60nm VO_2 continuous film on a silicon substrate, while for the metadevice, VO_2 nanoparticles were patterned and grown on Al_2O_3 and have a height of 37nm. These films were deposited at the same time but shadowing by PMMA reduces the height of the nanoparticles. The different substrate and thickness can both affect the grain size and grain boundary leading to deviations with the simulations. The VO_2 PT also depends on the nanocrystal size and it has been shown that nanocrystals result in a broader hysteresis loop and PT compared to thin films. Lastly, inhomogeneities in the fabricated bowtie antennas will broaden the resonances of the metadevice compared to the simulations.

4.4.3 Injection Current Dependence and Local Heating

From a materials perspective, VO_2 has a lower switching threshold than PCMs like GST due to the near-room-temperature PT. In order to electrically switch the device, a current is applied to the antenna layer through the bus bars, heating the metal (Figure 4.6a). Compared to external heaters, this technique only generates heat where it is required, reducing power consumption. The

38

measured optical properties, as a function of current injection, are shown in Figure 4.6b. Local Joule heating of the device results in the same modulation depth as using the temperature-controlled stage. The threshold current to switch the entire 24μm × 24 μm sample was found to be 56mA (2.2V), yielding a power consumption of 123.2mW, which agrees well with the calculated switching threshold (see A.4 for the simplified theoretical model).
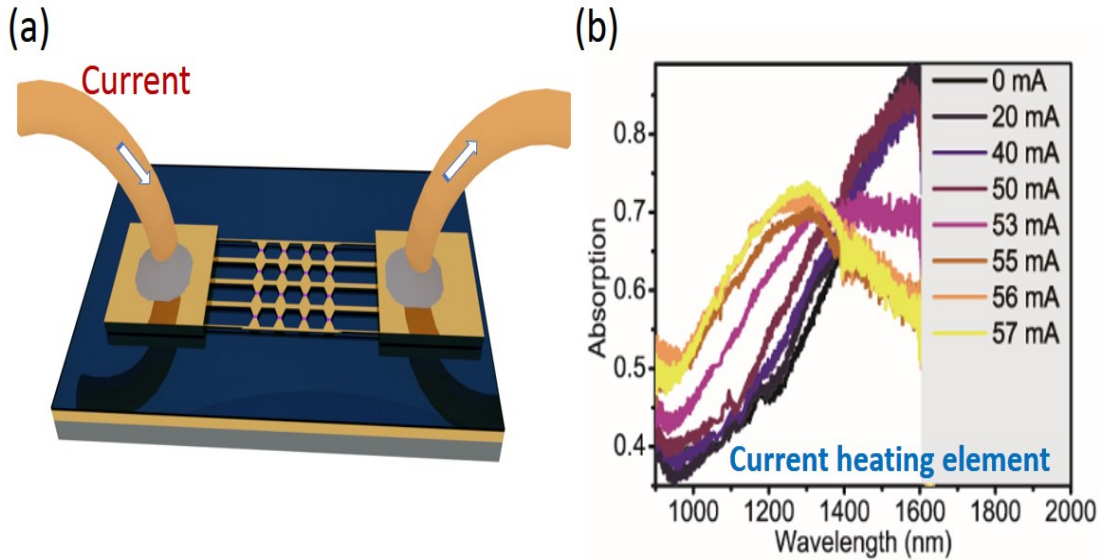
Figure 4.6 Local heating approach and injection current dependence. (a) schematic of the integrated heater with metal busbar connecting the bowtie antenna; (b) The MPA metadevice absorption spectra with different injection current.

4.5 Temporal Performance

The temporal response of the device was measured using a function generator to modulate the applied current while the reflectivity at 1107nm was monitored (see Figure 4.7a). The results are presented in Figure 4.7b. First, it should be noted that the modulation contrast of the temporal intensity measurements is 37%, matching the steady-state measurements in Figure 4.5a and indicating that the device is fully switched. Second, the reflected power follows the trigger signal and has a rise time of 2.3ms, which could be further reduced by increasing the applied current. The

relaxation time was measured to be 1.27ms, which is a function of the thermal conductivity of the substrate and the thermal capacitance of the VO_2. When plasmonic structures are fabricated on or under continuous VO_2 films, the absorption associated with the continuous VO_2 film increases insertion loss, reduces modulation depth, and lengthens response time. Here, the patterned nanocrystals have a thermal mass that is 18% that of a thin film of the same thickness. The substantially reduced thermal capacitance of the system results in a response time 400 times shorter than film-based metadevices while also lowering the power consumption of the device [115].
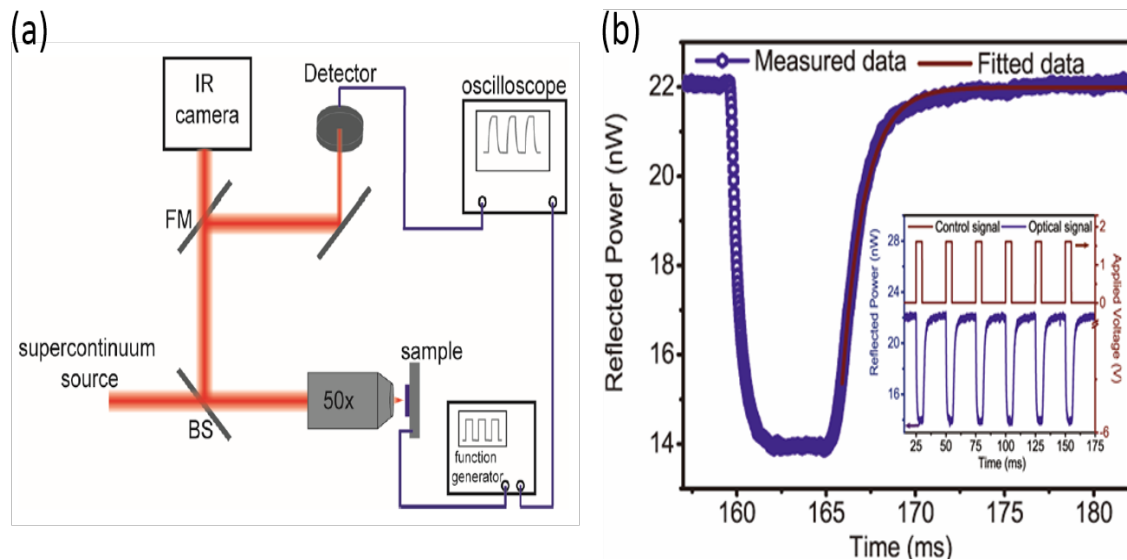
Figure 4.7 Temporal response characterizations. (a) Experiment setup for temporal measurements. Here BS and FM refer to a beam splitter and flip mirror, respectively; (b) Reflected power (blue circle) within one modulation cycle and the fitted exponential decay curve (red solid). The decay time is 1.27ms based on the fit. The inset shows the rigger signal (red right axis) and monitored reflection (blue, left axis) over multiple modulation cycles.

4.6 Demonstration of Spatial Control

To demonstrate spatially inhomogeneous metasurfaces, we first patterned a VO$_2$ nanoparticle array into the letters 'V' and 'U' and then overlaid these letters with a square, uniform, bow-tie antenna layer. The spectra of the bowtie antenna without VO$_2$, with semiconducting VO$_2$, and with metallic VO$_2$ in the feed-gap were measured and are show in Figure 4.8.
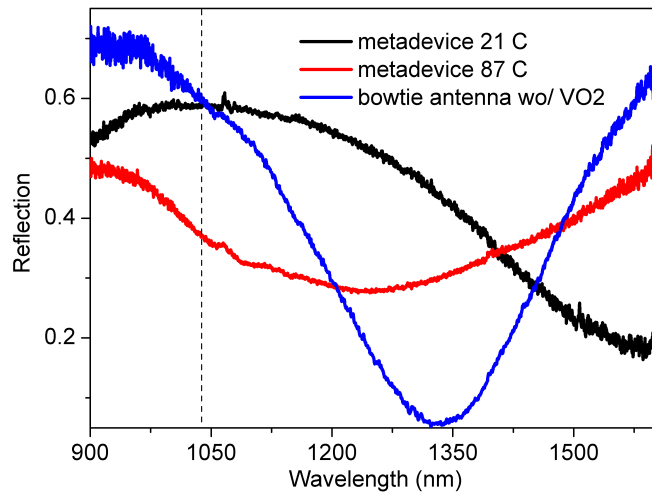
Figure 4.8 Measured reflection spectra for bowtie antenna without VO$_2$ in the feed-gap (blue curve), with semiconducting VO$_2$ (black curve), and with metallic VO$_2$ (red curve) in the feed-gap, respectively.

At a wavelength of 1010nm the antennas without VO$_2$, and with semiconducting VO$_2$, have identical reflection. This wavelength was chosen for illumination as the letters are hidden from view. Based on the measurements in Figure 4.8 the contrast in reflection is 23% between the antennas with and without VO$_2$ at 1010nm when the nanoparticles are transitioned to the metallic state.

One application of this approach could be in infrared and visible identification tags and coding. To demonstrate how one could employ the device for such applications, VO$_2$ nanocrystal arrays were patterned to form the letters 'V' and 'U' and then overlaid by a uniform, unpatterned,

bow-tie antenna layer (24μm × 24μm) (Figure 4.9a, d). The array was imaged at a wavelength of 1010nm, corresponding to the point where the bow-tie with semiconducting VO_2 in the feed-gap (30°C) have the same reflectivity as the bare bow-tie antenna array. In this case the array appears completely uniform. However, heating the metadevice to 82°C switches the VO_2 into the metallic state and shifts the absorption maximum to shorter wavelengths, resulting in a reflection contrast of 23%. As shown in Figure 4.9(c-d, e-f), this results in the "V" and "U" becoming visible, revealing the previously hidden image.
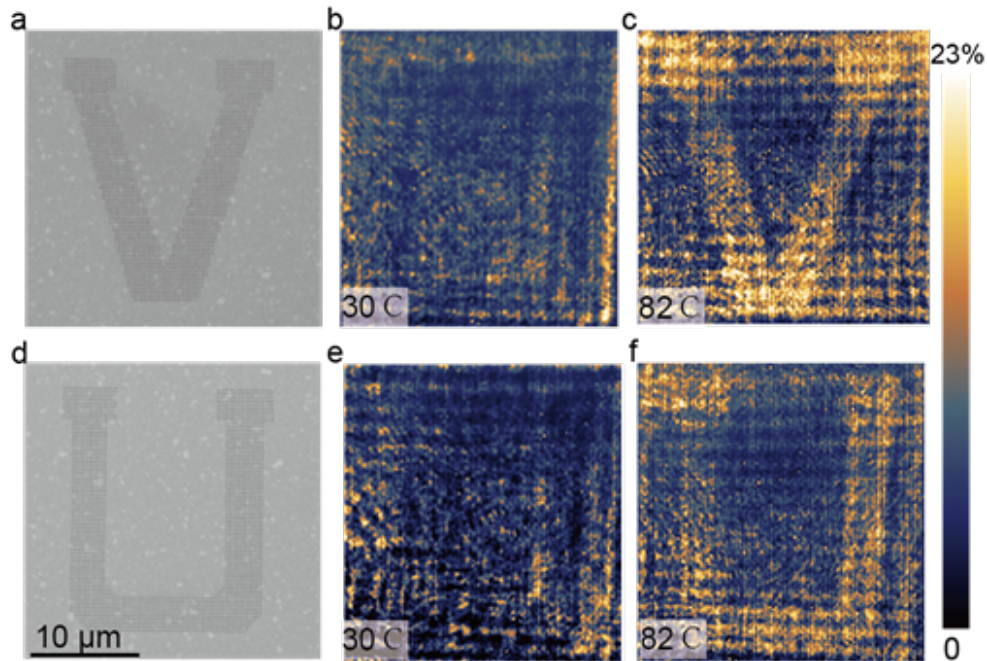
Figure 4.9 Dynamic metadevices displaying images. (a, d), VO_2 nanocrystal array in the shape of V and U. This array is covered with a uniform bow-tie antenna array. (b-c), (e-f), IR camera images of the final array at both 30°C and 82°C. The illumination wavelength is 1010nm. At this wavelength the MPA in the absence of VO_2 has the same reflection amplitude as an array with semiconducting VO_2 in the feed-gaps.

4.7 Conclusion

In this chapter, we have experimentally demonstrated that by combining decreased thermal mass phase change materials VO_2 and plasmonic field concentrator, an overall enhanced MPA metadevice performance is achieved. Aligned well with the FDTD simulation, we have significantly reduced the required switching time and power compared to other thin film-based spatial light modulators. As shown previously, the device exhibits a tuning range as large as 360nm and a modulation depth up to 33%, with a response time of 1.27 millisecond. All these figures of merit compare favorably with other reconfigurable metamaterials approaches. And the device response speed could potentially be improved to nanosecond by modifying the circuit layout and passing the current directly through the VO_2 nanocrystals. Other than triggering the PT with a temperature controlling stage or local resistive heater, the semiconductor-to-metal could also be triggered by the incident beam itself, leading to self-adaptive optical system, which is very important for sensitive optical element protection.

In addition, such configuration is not limited to bowtie antenna, it could also be used with other structures, such as gap in split-ring resonator, epsilon-near-zero (ENZ) mode, hybrid mode spacer and so on. And it could be further expanded to all dielectric metamaterials for complete transmission control or even phase modulation. And patterned GST phase change materials could also be integrated for non-volatile applications. We believe this reconfigurable metamaterial is a promising candidate for dynamic coatings and active beam shaping, and with further improvements in switching speed it could be employed for signal processing and display applications.

CHAPTER 5 NEAR INFRARED OPTICAL LIMITER BASED ON HUYGENS

METASURFACE DESIGN

5.1 Introduction

Development of passive optical power limiters for human eye and sensor protection is of growing significance as laser exposure is becoming more frequent in civilian and military scenarios. Ideally, the transmitted intensity of a passive optical limiter should be high at low light levels but adaptively clamp to nearly zero or a constant preset value once the input exceeds a specified threshold in order to protect the user or sensor. Laser goggles in use today rely on high constant absorption or reflection over a defined spectrum, which impair vision when the filtered laser line lies in the optical spectrum. Nonlinear optical limiting goggles can be designed such that they normally act as normal glasses with high transmission, reducing vision impairment, while in the event of an incident high-intensity laser, the nonlinear processes act to reduce power transmission below the eye damage threshold [177]-[180]. The near room temperature PT property of VO_2 naturally provides a well-defined thermal threshold for these kinds of applications. Studies also have shown that the VO_2 PT temperature can be increased or decreased by simply doping lighter or heavier atoms into the lattice, respectively [181][182]. However, developing VO_2-based coatings with large optical contrast, while still maintaining high on-state transmission is not possible if only relying on the material's intrinsic absorption contrast. This is due to the fact that a thick film would be needed to cut the transmission to nearly zero at the off state which would result in the on-state transmission also be greatly reduced.

In this chapter, a near infrared optical limiter based on a Huygens metasurface is demonstrated with a goal of maintaining high transmission in the on-state while dramatically damping the light when incident intensity rises over a critical level.

5.2 Huygens Metasurface and ENZ mode

5.2.1 Huygens Metasurface
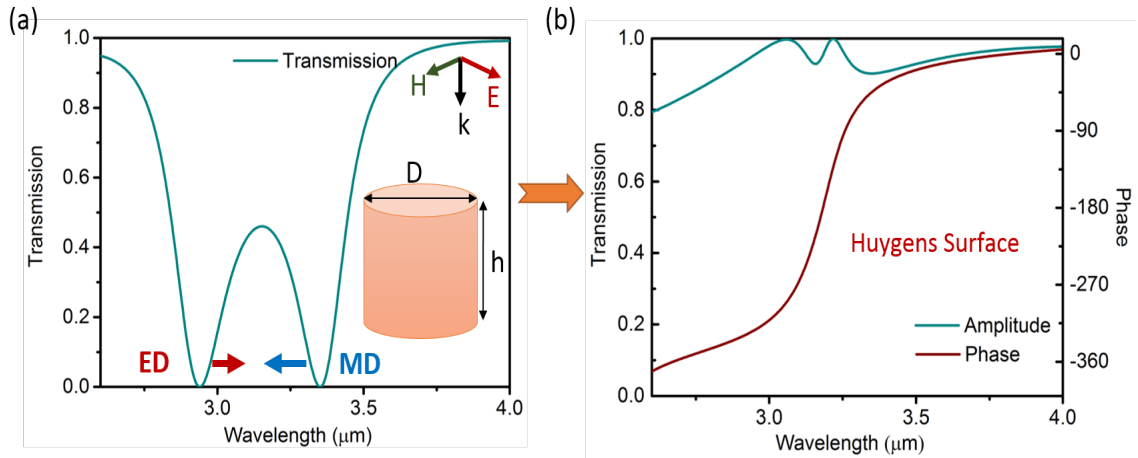
Figure 5.1 Huygens metasurface with Mie resonators. (a) The transmission spectrum shows the ED and MD resonances of a Mie resonator; (b) Transmission spectrum (blue curve) of a Huygens metasurface when the ED and MD are spectrally overlapped and result in 2π phase coverage (red curve).

For dielectric resonators, the locations of both the electric dipole (ED) and magnetic dipole (MD) resonances shift by changing the aspect ratio (AR) of the particle. With an optimized geometry, one can perfectly overlap the ED and MD resonances (Figure 5.1a). When this occurs, assuming these two dipole modes are of equal strength, the reflected fields from one dipole mode are out of phase with the other dipole mode, resulting in destructive interference and zero reflection. The absorption is negligible when the limiter is operated below the material bandgap. Thus, the metamaterial exhibits unity transmission (Figure 5.1b) [172]. Meanwhile, the phase accumulated by these both fundamental modes will be added together and shows a 2π change across the resonance. Metamaterials with this characteristic are called Huygens metasurfaces. A Huygens metasurface is not only achievable with Mie-type resonances, it can be also realized with multi-

45

layer plasmonic structures, and the metamaterial perfect absorber also belongs to the Huygens metasurface family [173]. All-dielectric Huygens metasurface also possess the field enhancement contributed from both ED and MD resonances, which makes it a potential candidate to integrate with active materials for realizing reconfigurable metamaterials.

5.2.2 ENZ mode

In order to further increase the absorption loss in the off-state and achieve a large modulation depth in the optical limiter, an ENZ mode can be used to concentrate light in the active media. Considering an interface between two media (media 1 and media 2), based on the electromagnetic boundary conditions, the displacement field normal to the interface should be conserved, which means $E_{z2}/E_{z1} = \epsilon_{z1}/\epsilon_{z2}$ assuming z is the normal direction to the interface. When $|\epsilon_{z2}| \ll |\epsilon_{z1}|$, the field in medium 2 is enhanced compared to the field in medium 1 [183]. The enhancement factor approaches infinity when $|\epsilon_{z2}|$ is 0 and this phenomenon is referred as an ENZ mode. ENZ modes can happen in plasmonic films where the frequency is close to the plasma frequency. The enhanced field leads to strong light-matter interaction which can be useful in applications such absorbers and active metamaterials as well as enhancing the coupling between electromagnetic fields and electrons in quantum-well systems [99][184]-[186]. The ENZ point of VO_2 is located around $\lambda = 1209$ nm in the metallic state which will be the wavelength at which we will design the optical limiter.

5.3 Metasurface Optical Limiter Simulated Results

In this work, the silicon-VO_2 nanostructures are designed on a SiO_2 substrate which has a refractive index $n_{Si} = 3.7$, $n_{SiO2} = 1.48$, and the VO_2 dielectric constant was obtained from

ellipsometry of a 60nm film on silicon at 25°C and 85°C. After optimization, the final dimensions are: lattice constant $p_x=p_y$=640nm, cylinder diameter D=432nm, silicon and VO_2 thickness h =180nm, t_{VO2}=30nm. The resonators are embedded in SiO_2 to provide a uniform index around the resonator. This symmetric design is critical to obtain ED and MD resonances of equal strength and obtain total destructive interference of the reflected electric field. When VO_2 is in the semiconducting state, the metamaterial will have a high transmission and when the VO_2 is switched to the metallic state, the increased loss, combined with enhanced electric field within the material will cause transmission to reach nearly 0. Figure 5.2c shows the transmission spectrum of the metamaterial optical limiter with metallic state VO_2 and Figure 5.2d shows the normalized electric field in the y and z directions.
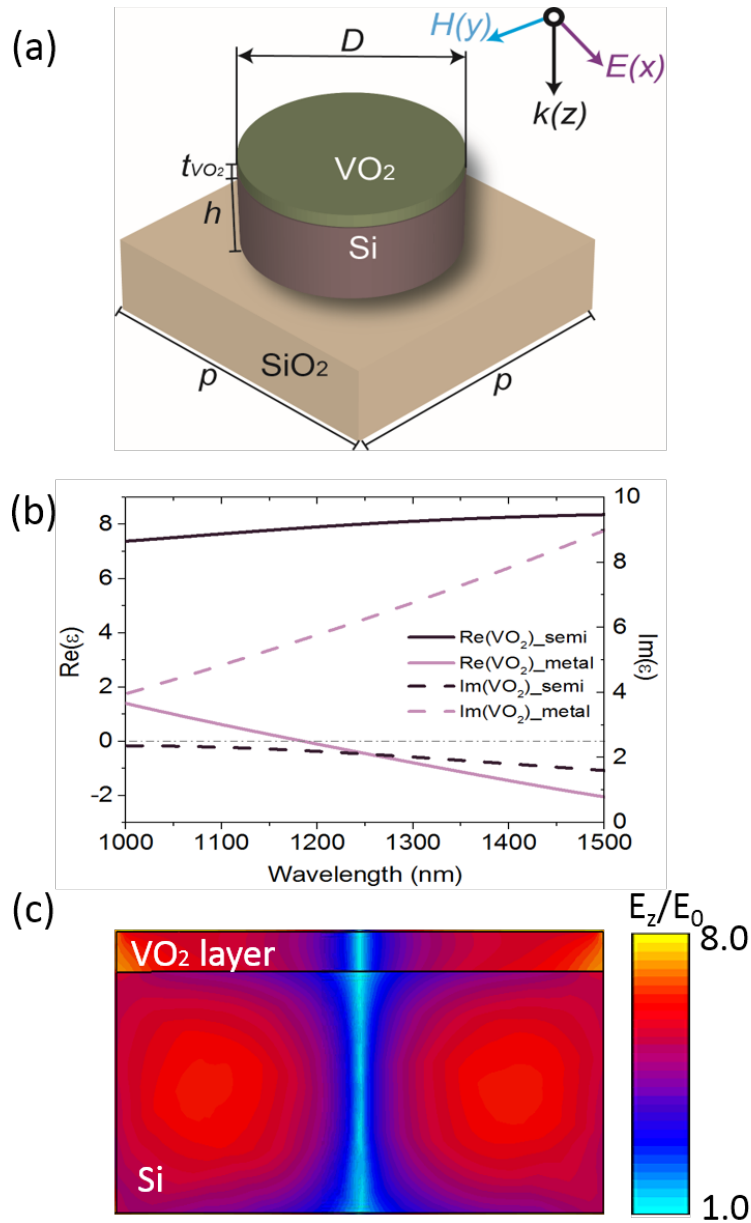
Figure 5.2 Near infrared optical limiter design based on Huygens metasurface mode and ENZ mode. (a) Schematic of the optical limiter metamaterials. The silicon high index cylinder is designed on the top of a SiO$_2$ substrate, with active materials VO$_2$ on the top. The structures is embedded in SiO$_2$. The dimensions are: lattice constant p=640nm, cylinder diameter D=432nm, silicon and VO$_2$ thickness h =180nm, t$_{VO2}$=30nm. (b) dielectric function of the VO$_2$ grown on a SiO$_2$ substrate measured in both semiconducting and metallic state; the ENZ mode happens around 1200nm; (c) Normalized electric field distribution profile for z directions calculated at the resonant wavelength of 1209nm.

In order to verify that the ED and MD are perfectly overlapped, transmission spectra were numerically calculated with different aspect ratio (AR=D/h) and are presented in Figure 5.3a-c. We can clearly trace the ED and MD resonances with semiconducting VO_2 until they are overlapped at an AR=2.4 (Figure 5.3a). At the overlap frequency there is a transmission of -3.6dB. In the metallic state the transmission drops to -41.8dB with a contrast of 38.2dB (Figure 5.3d). A resonance wavelength blue shift was also observed due to a small disturbance of the ED and MD overlap caused by the change in VO_2 permittivity.
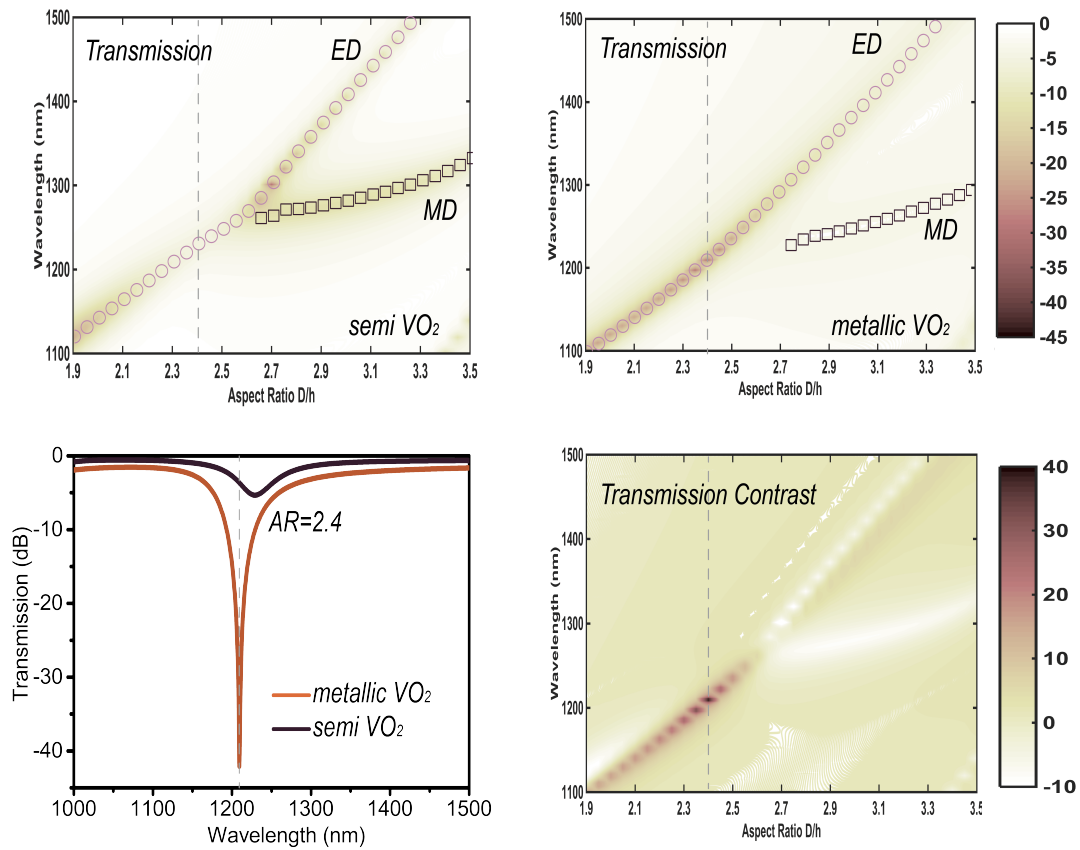
Figure 5.3 Numerically calculated transmission intensity of the metamaterial optical limiter. (a) transmission of the metamaterial in semiconducting state with different AR, which shows ED and MD merging to form a Huygens metasurface at AR=2.4; (b) transmission of the metamaterial in metallic state; (c) transmission contrast; (d) Spectra of the metamaterial at AR=2.4, with VO_2 in both semiconducting state and metallic state.

49

5.4 Intensity Dependence

In order to determine the input power threshold to trigger the PT, the CST thermal solver was employed, using the material properties listed in Table 5.1. Assuming the silicon and SiO$_2$ are lossless, the incident power is assumed to be absorbed within the VO$_2$ nanoparticles, with normalized absorption $A_{@semi} = 0.567$ and $A_{@metal} = 0.898$ which are acquired from the absorption spectra in Figure 5.4 at $\lambda = 1209nm$. The VO$_2$ is treated as a volumetric heat source in the unit cell with heat dissipated through the substrate as well as the surroundings. To simplify the model and estimate the max power to trigger the phase transition of the VO$_2$, an ambient air convective heat transfer coefficient of $50W/m^2$ /K (CST default value for air) is used to replace the SiO$_2$ index matching medium. Adiabatic boundaries are used in the in-plane directions to mimic a periodic boundary condition.
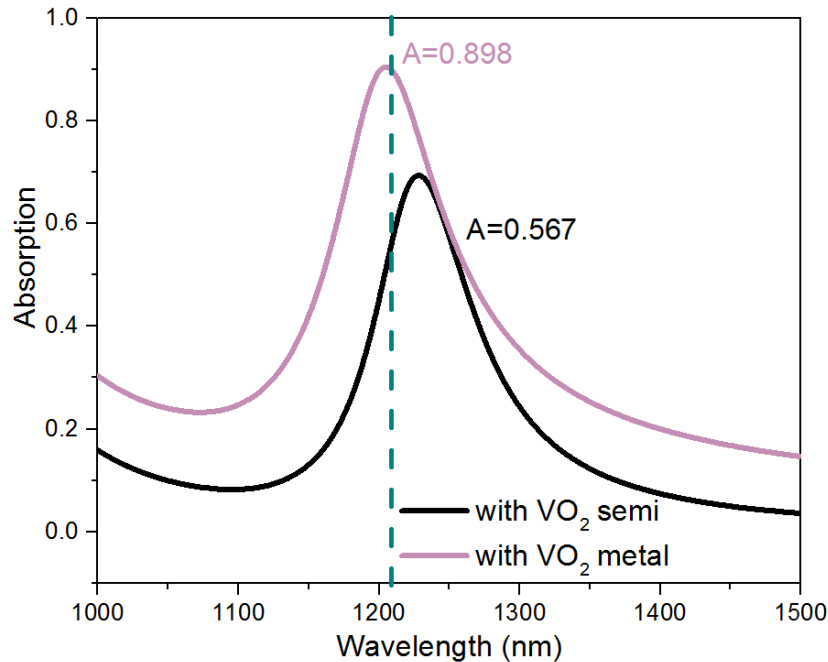
Figure 5.4 Absorption spectra of the metamaterial optical limiter. At 1209nm, the absorption coefficients are read to be A=0.567 and 0.898 in the semiconducting and metallic state VO$_2$, respectively.

In the semiconducting state, the mean temperature of VO_2 is heated to 65°C at an incident power of 15µW. Once the PT is triggered, the temperature will rise with a steeper slope (Figure 5.5a) due to the increased absorption. After switching there is a sudden drop in the transmission, which will dramatically lower the transmitted power by more than three orders of magnitude (Figure 5.5b).

Table 5.1 Thermal properties of the materials in the metamaterial optical limiter design

Materials	Density (g/cm^3)	Thermal Cond. (W/K·m)	Heat Capacity (kJ/K·kg)
silicon	2.328	1.5	0.71
VO_2 (85 °C)	4.65	6	0.78
VO_2 (25 °C)	4.57	3.5	0.656
SiO_2	2.4	1.4	0.75
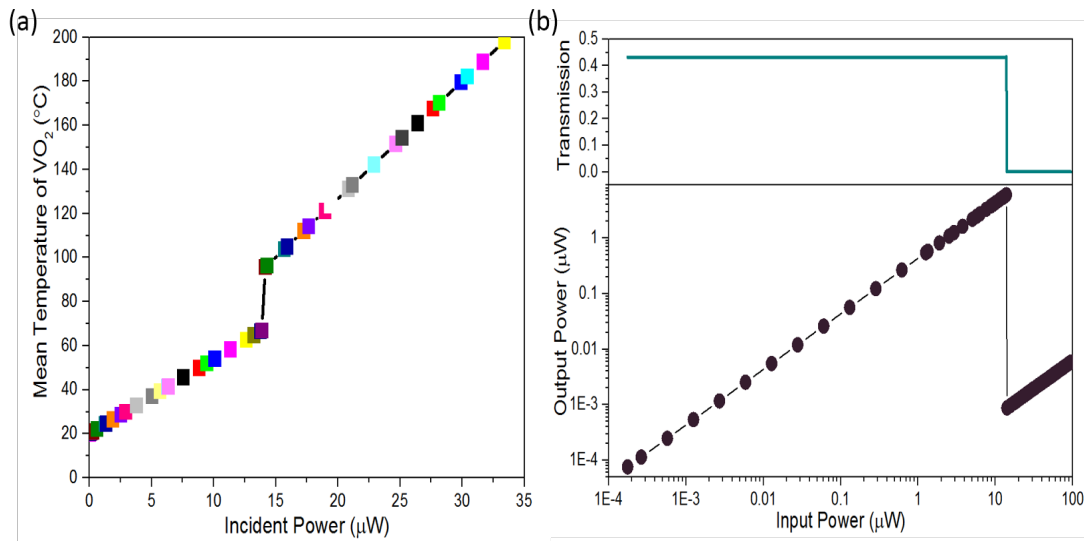
Figure 5.5 Intensity dependence of the metamaterial optical limiter response. (a) Simulated mean temperature of the VO_2 nanostructures with different incident power; (b) Nonlinear relation between the metamaterial's transmission and input power (top panel), output power and input power (bottom panel).

51

For a single unit cell, the power threshold needed to activate the PT is about 15µW. Considering a uniform metamaterial array with 20µm × 20µm size (~976 unit cells), the total beam power and intensity are calculated to be 14.65mW, which is consistent with the fluence needed for ultrafast VO_2 PT trigged by a femtosecond laser pump (44mW for beam spot 30-50µm) [187]. This value is nine times smaller than the thermal triggering of the VO_2 in chapter 4 (126mW) (A. 4). One reason is that the dielectric has nearly zero absorption loss and all of the incident power is used to heat up the VO_2 material. This is different than in plasmonic metamaterials where the metal absorbs a large amount of the energy. Metal structures also conduct heat well and the bowtie antenna and VO_2 nanoparticle array was totally exposed to air, which has a better convection than SiO_2 capsulated Huygens metasurface cylinders here.

5.5 VO_2 thickness Dependence and Angle Dependence

In this Huygens metasurface optical limiter design, the response is very sensitive to the VO_2 active layer thickness. If the VO_2 is too thick, on-state transmission will be reduced and the cutoff contrast will be reduced. The reason for this is that the ENZ mode plays a more minor role as the film thickness increases. To illustrate the role of the VO_2 thickness, a numerical simulation was performed with the same geometry as Figure 5.2a, while varying the VO_2 thickness from 5nm to 35nm.
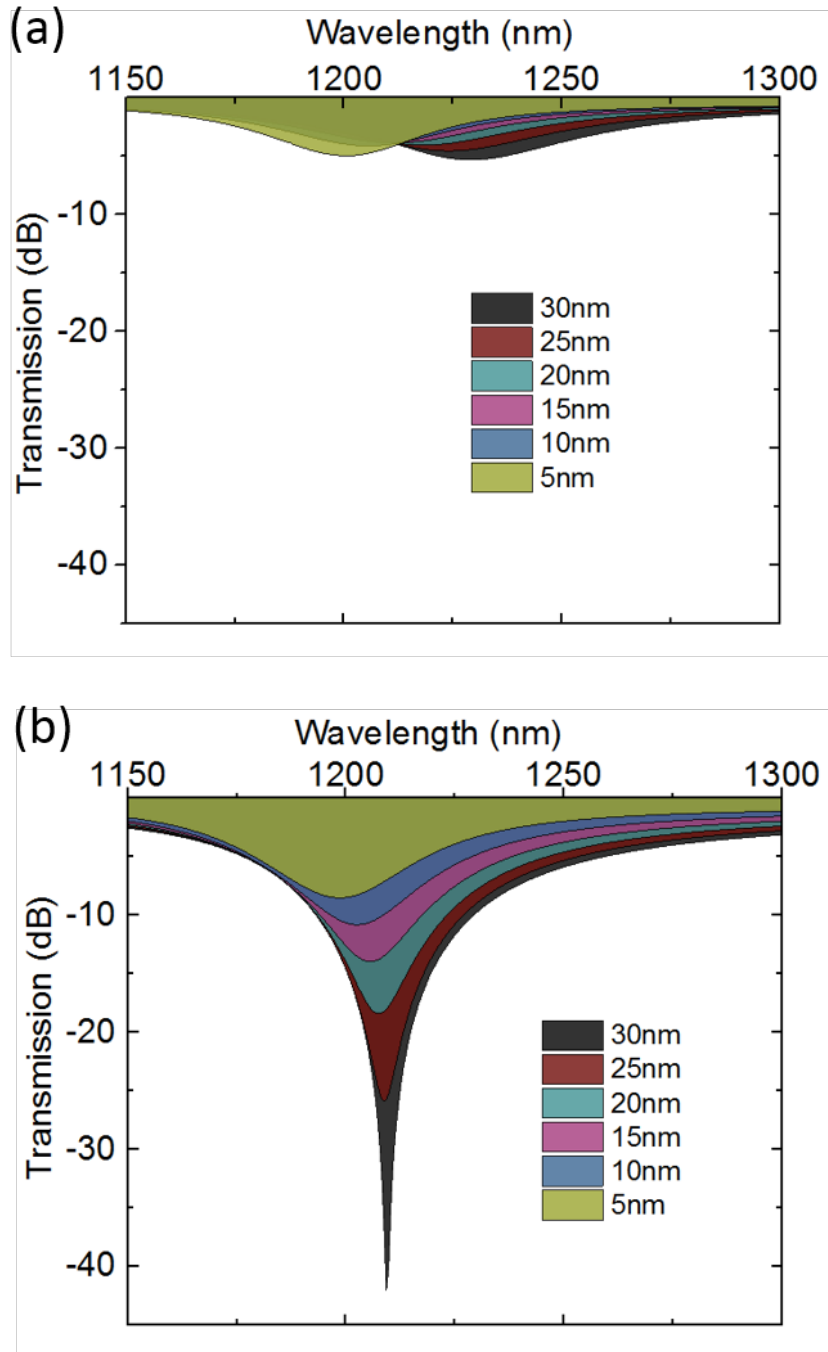
Figure 5.6 VO$_2$ thickness dependence. (a) Simulated transmission spectra with semiconducting state VO$_2$, the thickness is varied from 5nm to 30nm. (b) Simulated transmission spectra with metallic state VO$_2$.

The VO$_2$ thickness dependence plots in Figure 5.6 demonstrate that the metamaterial transmission decreases with thicker VO$_2$ for both the semiconducting and metallic state. For the semiconducting state the change is smaller due to the limited loss of the material. For the metallic state, the change in the transmission is larger due to the spectral mismatch in the ED and MD as well as the increased loss. If the VO$_2$ thickness in increased to 35nm, the contrast will drop (Figure 5.7), indicating 30nm of VO$_2$ is the optimal thickness to maintain the Huygens metasurface and ENZ mode. To emphasize the importance of the field enhancement from the dielectric resonators, simulated on-off contrast based on a VO$_2$ film with the same thicknesses has been given in Figure 5.7. The data are multiplied by a factor of 5 to fit the scale. With 30nm VO$_2$, the on-off contrast is improved by as much 38.0 dB.
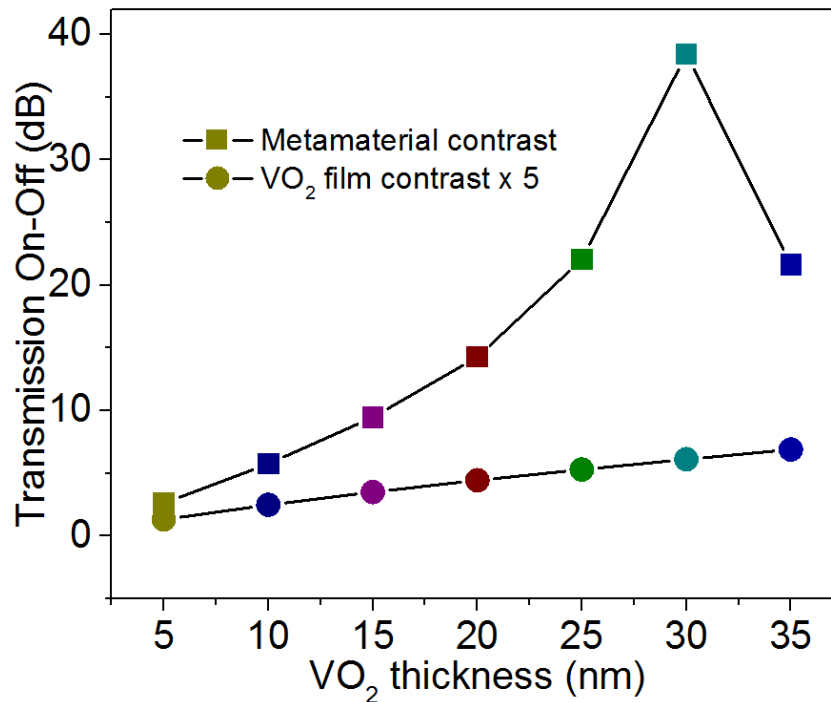
Figure 5.7 Transmission contrast with varying VO$_2$ thickness for the metamaterial optical limiter (solid square) and VO$_2$ continuous film (solid circle).

Our metamaterial optical limiter is made of cylinders which operate for all of the incident polarizations. However, Huygens metasurfaces are generally not suitable for wide incident angle since the ED and MD resonant positions are affected by the incident angle. In Figure 5.8 the transmission spectra of the metamaterial optical limiter are calculated at different angles of incidence. For angles larger than 15°, the ED and MD are clearly separated to two spectra dips with lower transmission at the designed wavelength of 1209nm (Figure 5.8a). With metallic state VO_2 (Figure 5.8b), the transmission rises to -15.0dB for angles of 15° and 20°. As a result, the overall contrast is also decreased.
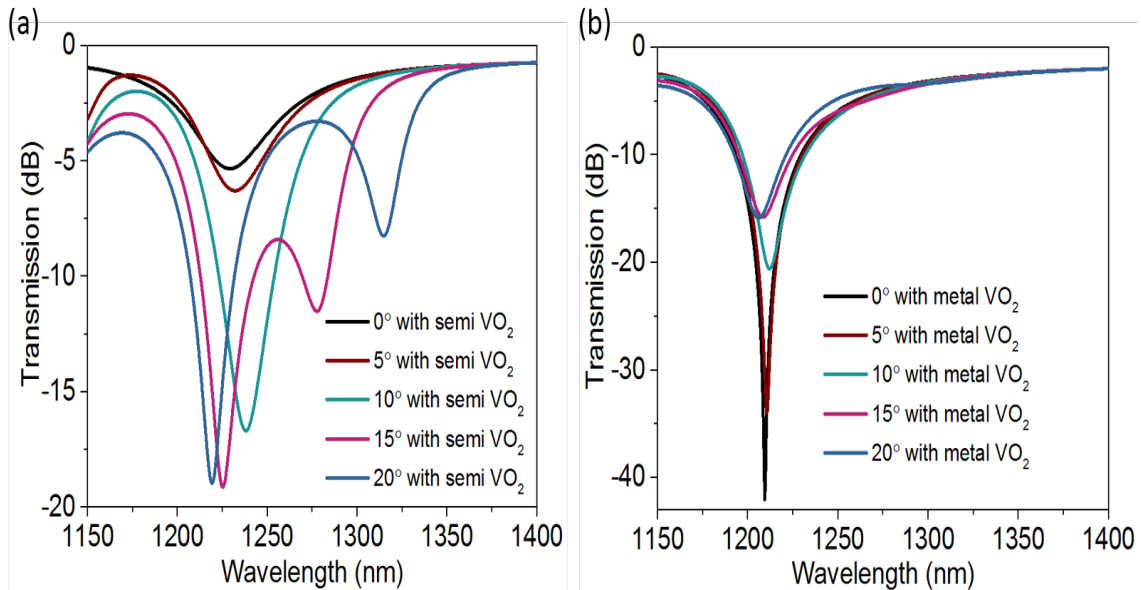
Figure 5.8 Angle dependence of the metamaterial optical limiter. Transmission spectra with (a) semiconducting VO_2 (b) metallic VO_2 with incident angles changing from 0 to 20 degree.

5.6 Expanding to Other Wavelengths

One advantage of metamaterials is that we can tune the structure dimensions to adjust the working frequency. For this metamaterial optical limiter, the ENZ point is fixed around 1200nm.

Though the ENZ point might be tunable by doping, scarcely any *systematic* research has been done on VO_2 with different dopants and doping levels. However, even without the ENZ effect, this approach can still work with a slight decrease in the on-off contrast. To explore how this type of metamaterial operates at other wavelengths, the transmission spectra are calculated with all geometry dimensions scaled with a ratio *s*, except that the VO_2 thickness is constant at 30nm. The resonance wavelengths are adjusted to around 1064nm, 1350nm, 1550nm and 1850nm with a scale factor of 0.9, 1.1, 1.3, and 1.5, respectively (Figure 5.9). An on-off modulation depth of 25.0 dB is observed for all the four metamaterials. The decreased contrast also indirectly proves that the ENZ mode helps with better field concentration and high cutoff efficiency.
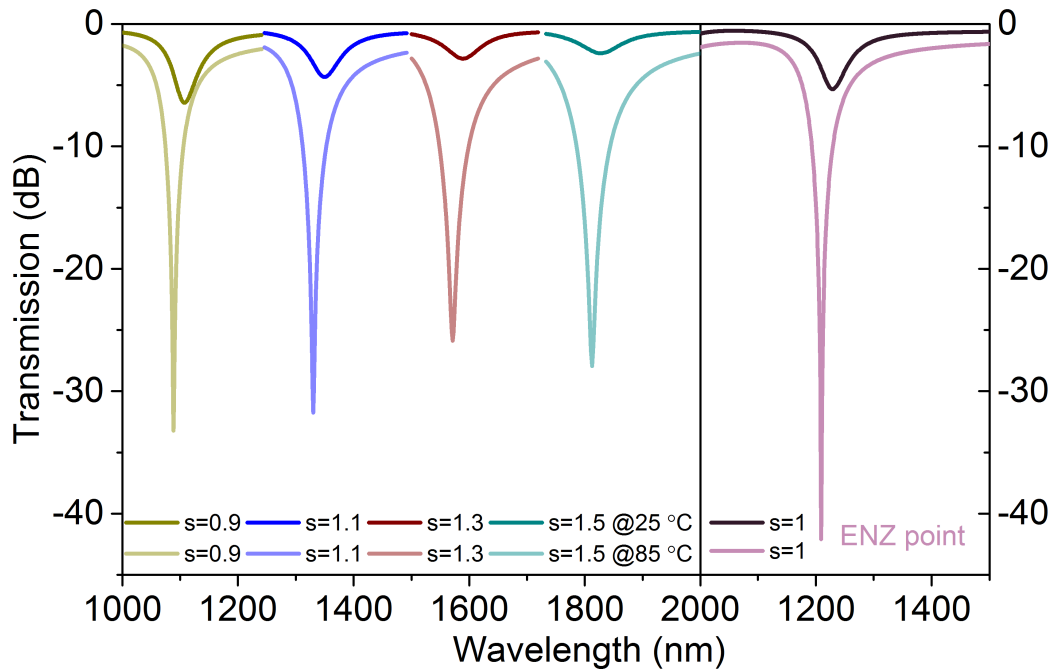
Figure 5.9 Transmission spectra for metamaterial optical limiter design working at different wavelengths. The overall geometry is equally adjusted with a scale s=0.9, 1.1, 1.3 and 1.5 to work near 1064nm, 1350nm, 1550nm, and 1850nm, respectively.

5.7 Conclusions

In this chapter, a metamaterial optical limiter is demonstrated through numerical simulations. This design adds an additional epsilon-near-zero mode to the Huygens metasurface platform. Due to the large permittivity change at the silicon/VO_2 interface, further confinement of the electric field within the thin VO_2 nanostructures volume is achieved, which leads to a 38.2dB transmission on-off contrast at the Huygens metasurface resonant wavelength. To estimate the incident power threshold for this self-adjustable optical device, a thermal steady state solver was used to calculate the temperature of the VO_2, which allowed a prediction for the power threshold of around 14 mW for an area of 20μm × 20μm. This value is consistent with previous works and could be modified by doping the VO_2 or triggering the PT with an ultrafast laser pulse. The VO_2 thickness was optimized at 30nm considering all of the factors such as the VO_2 intrinsic absorption coefficient, ED and MD coupling in the Huygens metasurface, and the ENZ effect. Simulations also show that this optical limiter could be adjusted to work at other frequencies with a slight decrease in modulation depth.

CHAPTER 6 CONCLUSION AND OUTLOOK

The focus of this research has been the development of functional optical devices based on platform consisting of metamaterials combined with VO_2. The development of metamaterials offers us the ability to achieve specific features such as engineered anisotropy, enhanced field concentration, and wavefront tailoring at any particular optical wavelength by modifying the subwavelength structures. The strongly correlated material, VO_2, exhibits near room temperature semiconductor-to-metal PT, which makes it an ideal candidate in applications in reconfigurable optics, smart windows, as well as data buffering and storage. In this work, I outlined my efforts to efficiently integrate small thermal mass VO_2 into metamaterials nanostructures, realizing full control of reflection, absorption, and transmission. In this chapter, I will first summarize all of the results and then provide some insight into future directions.

6.1 Summary

In chapter 4, a plasmonic perfect absorber architecture is implemented to completely block transmission and engineer the absorption of a metamaterial system. A bowtie antenna was selected based on its extreme electric field confinement in the feed-gap which was used to amplify the effect of the semiconductor-to-metal PT in embedded VO_2 nanostructures. As a result, large resonant wavelength shift and reflection magnitude tuning were experimentally observed. By connecting the bowtie structures to form a local resistive heater, we further demonstrated that the decreased thermal mass of the VO_2 contributes to a faster response time and lower power consumption per bit, which are also critical factors in the performance of an optical modulator.

In chapter 5, an all-dielectric metamaterial platform was utilized, aiming at realizing complete control over the amplitude of the transmitted light in near infrared wavelength. For the fundamental modes of high refractive index structures, ED and MD resonances, the switching

ability is limited if we solely utilize one of them. When we spectrally overlap the two resonances together and form a Huygens metasurface, the destructive interference of the two modes leads to minimum reflection and nearly unity transmission in the on-state. We have demonstrated that an ENZ mode also helps with squeezing field into an ultrathin VO_2 film, which increased the metamaterial absorption in the off-state and reached a cutoff efficiency of 38.2dB. Thermal steady state simulations were performed to calculate the cutoff threshold for the incident power at the resonance wavelength of 1209nm, close to the ENZ point. The reported value of 14mW for a 20μm $\times$ 20μm array aligned well with previous works engaging VO_2 PTs triggered with optical methods. In specific conditions, this threshold is tunable by doping or applied stress. The device response was proven to be dependent on the VO_2 thickness and is sensitive to the incident angle.

6.2 Future Avenues

Although the VO_2 PT has been studied for more than half a century, designing optical devices for operation in free space is still a challenge. This dissertation work proves that combining phase change materials with nanoscale metamaterials is a promising research direction for this purpose. In my opinion, there are a few avenues to expand on this. To begin, integrating VO_2 nanoparticles with field concentrators can be used to realize optical devices for amplitude control with excellent performance, which have been partially demonstrated in this dissertation. Meanwhile the field concentrators can be used to concentrate incident light intensity in a small spot and selectively expose a photoresist, which could be used to eliminate the overlay steps in lithography and lead to large scale fabrication of these functional devices. Though VO_2 mainly exhibits large dielectric function contrast at infrared wavelengths, it can possibly be used in the visible region for dynamic color change applications since the resonance frequency is extremely sensitive to subtle permittivity changes. In addition to amplitude modulation, VO_2 based reconfigurable metamaterials

can also be used to realize control over the wavefront and polarization, which have not yet been investigated.

Vanadium dioxide is a very good candidate for bolometers or photodetectors based on the dramatic resistivity contrast across the semiconductor-to-metal PT. Metamaterial perfect absorbers can fully collect the incident photons, turn the energy into heat and trigger the semiconductor-to-metal transition. With some modifications to the metal structure's architecture we can potentially read the electric signal from this event. Pristine VO_2 has a sharper PT hysteresis which is good for binary detection while doped VO_2 has a more gradual slope suitable for analog signals. These reconfigurable devices can serve as a thermochromic coatings for thermal management applications. With the help of metamaterials, the overall emissivity can be altered between 0 and 1. This engineered thermal emissivity can maintain a constant temperature or could be used to magnify the signal for better image recognition.

A.1 Methods

A.1.1 Simulation

Finite-difference-time-domain simulations were performed with a commercial software package, CST microwave studio. For the uniform metamaterials array, simulations of the spectra magnitude and phase were run at one unit cell under the frequency domain solver, with plane wave excitation signal and periodic in-plane boundary conditions and perfectly matched layers out-of-plane boundary conditions. The optical properties of gold were taken from Johnson and Christy [188] though the damping was tripled compared to that of bulk gold to more closely match the experimental results. And VO_2 dielectric functions were imported from ellipsometry measured data.

A.1.2 VO_2 Elliposometry Measurement and Modeling
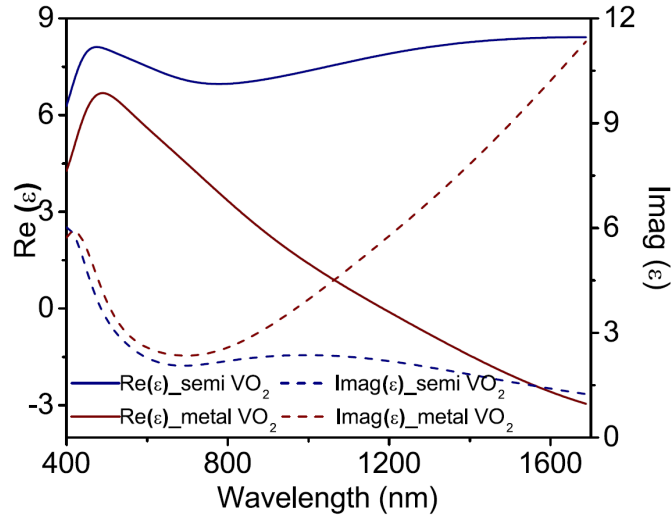
Figure A. 1 Measured permittivity of a sputtered VO_2 thin film on a silicon substrate in semiconducting (25°C) and metallic state (85°C).

To measure the VO_2 dielectric function, J.A. Woollam spectroscopic ellipsometer was used to collect the Fresnel reflection coefficients for *p-* and *s*-polarized light at three angles (60°, 65° and 70°) at temperatures of 25°C and 85°C. The M2000 ellipsometer with heated stage accessory recorded data from 0.4-1.7μm. The measured data were modeled with CompleteEASE software from J.A. Woollam with a silicon substrate layer, 3nm native oxide layer and 60nm thick oscillator layer. For this near infrared data, up to four Lorentz oscillators were used to reach a mean-square error (MSE) smaller than 10 (Figure A. 1).

Additional optical characterization was performed with the homemade white light hysteresis setup which records the overall transmitted or reflected intensity (Figure A. 2). The ability for the VO_2 thin films to switch was confirmed with the contrast above and below the PT threshold. To make sure the closest property matching between the witness VO_2 film and the VO_2 nanostructures embedded in the metamaterials, all of these films were deposited and annealed together with same growing and annealing conditions.
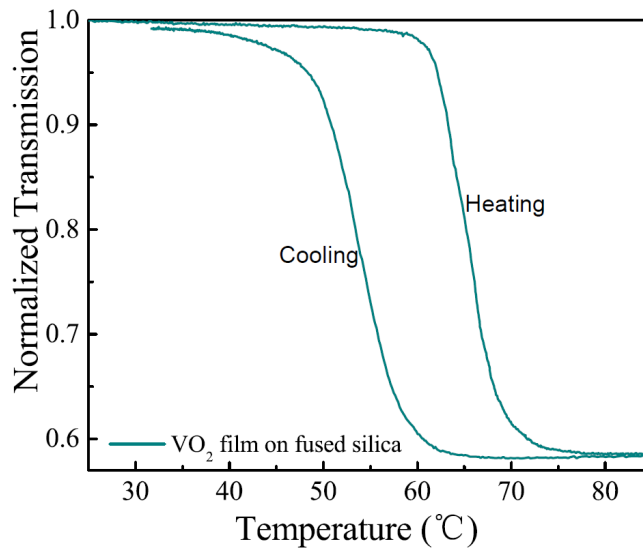
Figure A. 2 Normalized while light transmission hysteresis of a RF sputtered VO_2 thin film on a SiO_2 substrate.

62

A.2 Gap Size Dependence

The antenna gap size is an important parameter in the metamaterial design. In the case of VO₂ nanoparticles in the semiconducting state, reducing the gap width will increase the capacitance in the gap and significantly shift the resonance to longer wavelengths. In the case of metallic VO_2, the capacitive gap is largely shorted as VO_2 is more conductive, so reducing the gap results in a much smaller change in the resonance frequency. To investigate the gap size dependence of our metadevice, we have simulated the response for gap widths ranging from 30nm to 80nm while keeping the other dimensions constant. The results for semiconducting VO_2 are shown in Figure A. 3a while the metallic state is shown in Figure A. 33b. These results confirm the description above and show that smaller gap sizes result in larger modulation depth (Table A. 1).
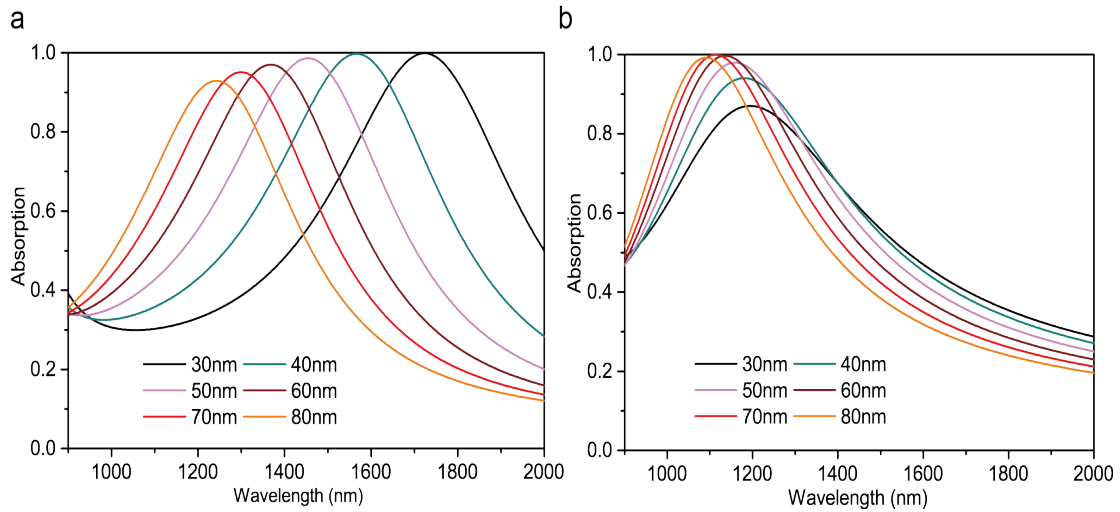
Figure A. 3 Simulated absorption spectra with varying gap size for (a) semiconducting VO_2 nanoparticles (b) metallic VO_2 nanoparticles.

Table A. 1 Simulated wavelength tuning and modulation depth with different gap sizes.

Gap size (nm)	30	40	50	60	70	80
Wavelength tuning (nm)	524	375	295	232	182	149
Modulation depth	61%	51%	42%	33%	25%	22%

Note: The modulation depth here is calculated at the resonant wavelength when the VO_2 nanoparticles are in the semiconducting state.

A.3 Thin Film Stack Thermal Stability Analysis and Test

When film thickness is less than 10^{-4} times the substrate thickness (for example, film thickness smaller than 50nm on a 500um substrate), the thermal stress caused by annealing can be estimated using a one-dimension approximation [189]:

$$\sigma_{th} = E_f \left(\alpha_f - \alpha_s \right) \left(T_s - T_a \right) \tag{A.1}$$

Here, σ_{th}, E_f, α_f, α_s, T_s, and T_a stands for stress, Young's modulus, film thermal expansion coefficient, substrate thermal expansion, substrate temperature, and processing or measurement temperature, respectively. A positive σ_{th} corresponds to a tensile stress. In our case, the sputtered VO_2 thin film or patterned structure has to be annealed at 450°C for 5 min, in a 250mTorr O_2 environment. Any thermal expansion mismatch between the MPA backing mirror and substrate could lead to cracking and leakage current preventing electrical control of the structure. We considered four combinations of two noble metals (Ag, Au) and two substrates (Si, fused SiO_2) to get an optimized design for the MPA configuration. Only the combinations in which stress is less than the yield stress (see Table A. 2 for material properties) will survive the annealing procedure.

Table A. 2 Properties of coating and substrate materials

	Melting Point (°C)	Young's Modulus (GN m^{-2})	Yield strength (GN m^{-2})	α_f (10^{-5} °C^{-1})
Ag	961	83	0.055	1.8
Au	1064	79	0.21	1.62
Si	1414	130-188	NA	0.256
SiO$_2$	1650	71.7	NA	1.23

Based on a deposition temperature of 40°C and an annealing temperature of 450°C the film stresses were calculated to be:

$$\sigma_{Ag\ on\ Si} = 0.525\ GN\ m^{-2} > 0.055\ GN\ m^{-2}$$

$$\sigma_{Ag\ on\ fused\ silica} = 0.194\ GN\ m^{-2} > 0.055\ GN\ m^{-2}$$

$$\sigma_{Au\ on\ Si} = 0.44\ GN\ m^{-2} > 0.21\ GN\ m^{-2}$$

(A.2)

$$\sigma_{Au\ on\ fused\ silica} = 0.126\ GN\ m^{-2} < 0.21\ GN\ m^{-2}$$

Both the calculations and experimental tests (see Figure A. 4) showed that a gold film on a fused silica was the best option.
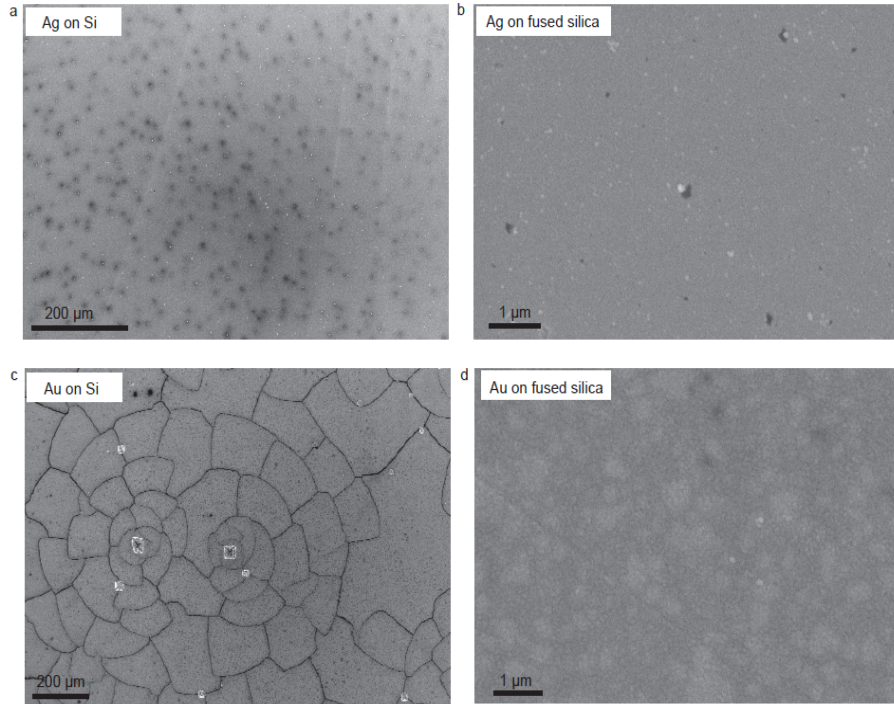
Figure A. 4 SEM image of (a) Ag on Si; (b) Ag on fused silica; (c) Au on Si; (d) Au on fused silica after the sample was annealed for 5min in O_2 at 450°C, (VO$_2$ annealing condition).

A.4 Calculation of Local Heating

To acquire a rough estimate of the required thermal power for switching the metamaterial, a simple heat transfer model, $q = 2Dk(T_{high} - T_{low})$ based on shape factors is used here, where *q, D, k,* and *T* stand for input power, array diameter, substrate thermal conductivity and temperature, respectively. The calculated switching power is 99mW, assuming the total array area is uniformly heated from 20°C to 85°C and that heat is only dissipated through the substrate. This model neglects convective heat transfer and assumes the system is in steady state. This value compares favorably with the measured value of 123.2 mW.

APPENDIX B

B.1 Methods

B.1.1 Simulation

Finite-Difference-Time-Domain simulations were performed with a commercial software package, CST microwave studio. For the uniform Huygens metasurface array, simulations of the spectra magnitude and phase were run at one unit cell under the frequency domain solver, with plane wave excitation signal and periodic in-plane boundary conditions and perfectly matched layers out-of-plane boundary conditions. The whole device was embedded in SiO_2 material with index of 1.48. Silicon is modeled as lossless with an index of 3.7. The VO_2 dielectric functions were imported from ellipsometry measured data.

A CST thermal solver was used to calculate the cutoff threshold for the optical limiter based on an assumption that both silicon and SiO_2 are lossless and the incident power is absorbed within the VO_2 nanoparticles, with normalized absorption $A_{@semi} = 0.567$ and $A_{@metal} = 0.898$. These absorptions were read from the absorption spectra at $\lambda = 1209.3nm$. The VO_2 solid is treated as a volume heat source in the unit cell with heat dissipated through the SiO_2. At the SiO_2/Air interface the convection was set to be 50W/m^2 /K. Adiabatic boundaries are used in the in-plane directions to mimic a periodic boundary condition.

B.2 Simulated Results Plotted in Linear and dB Scale

For a better comparison, we plotted the absorption, transmission and reflection spectra of the Huygens metasurface optical limiter in Figure B. 1, with linear and dB scale. Both semiconducting and metallic VO_2 were considered here.
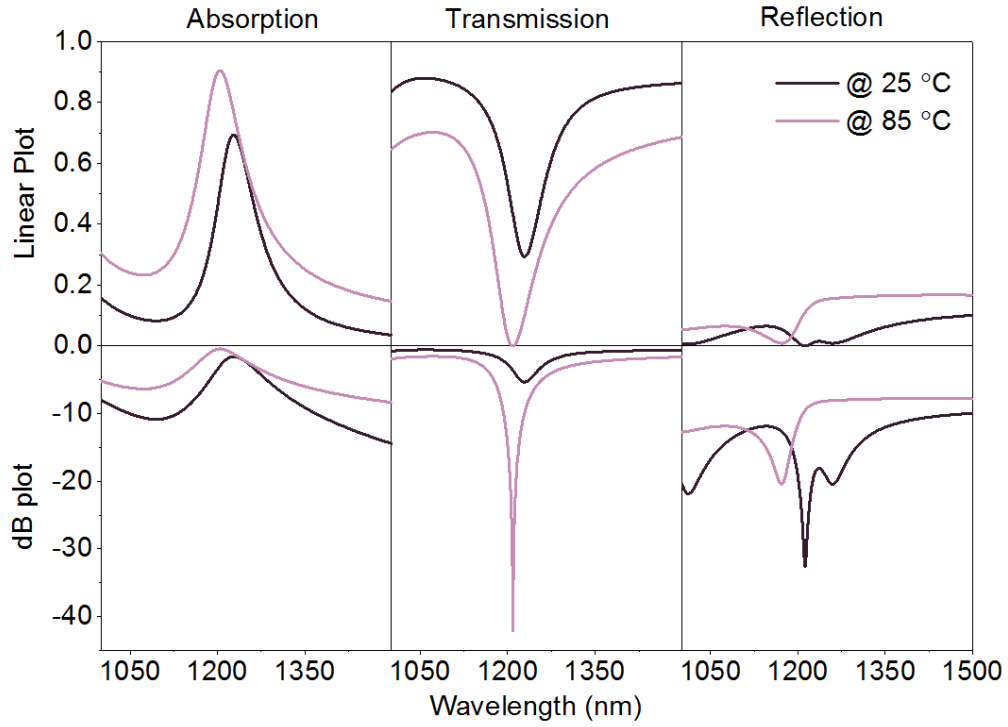
Figure B. 1 Simulated absorption, transmission, reflection spectra for the Huygens metasurface optical limiter, plotted in linear and dB scales.

BIBLIOGRAPHY

[1] Liu, Yongmin, and Xiang Zhang. "Metamaterials: a new frontier of science and technology." *Chemical Society Reviews* 40.5 (2011): 2494-2507.

[2] Pendry, John B., et al. "Magnetism from conductors and enhanced nonlinear phenomena." *IEEE Transactions on Microwave Theory and Techniques* 47.11 (1999): 2075-2084.

[3] Shelby, Richard A., David R. Smith, and Seldon Schultz. "Experimental verification of a negative index of refraction." *Science* 292.5514 (2001): 77-79.

[4] Jacob, Zubin, Leonid V. Alekseyev, and Evgenii Narimanov. "Optical hyperlens: far-field imaging beyond the diffraction limit." *Optics Express* 14.18 (2006): 8247-8256.

[5] Salandrino, Alessandro, and Nader Engheta. "Far-field subdiffraction optical microscopy using metamaterial crystals: Theory and simulations." *Physical Review B* 74.7 (2006): 075103.

[6] Govyadinov, Alexander A., and Viktor A. Podolskiy. "Metamaterial photonic funnels for subdiffraction light compression and propagation." *Physical Review B* 73.15 (2006): 155108.

[7] Liu, Zhaowei, et al. "Far-field optical hyperlens magnifying sub-diffraction-limited objects." *Science* 315.5819 (2007): 1686-1686.

[8] Zhang, Xiang, and Zhaowei Liu. "Superlenses to overcome the diffraction limit." *Nature Materials* 7.6 (2008): 435.

[9] Li, Wei, and Jason Valentine. "Metamaterial perfect absorber based hot electron photodetection." *Nano Letters* 14.6 (2014): 3510-3514.

[10] Chen, Tao, Suyan Li, and Hui Sun. "Metamaterials application in sensing." *Sensors* 12.3 (2012): 2742-2765.

[11] Wang, Wenyi, et al. "Hot electron-based near-infrared photodetection using bilayer MoS2." *Nano Letters* 15.11 (2015): 7440-7444.

[12] Li, Wei, and Jason G. Valentine. "Harvesting the loss: surface plasmon-based hot electron photodetection." *Nanophotonics* 6.1 (2017): 177.

[13] Stewart, Matthew E., et al. "Nanostructured plasmonic sensors." *Chemical Reviews* 108.2 (2008): 494-521.

[14] Zhu, Zhihua, et al. "Broadband plasmon induced transparency in terahertz metamaterials." *Nanotechnology* 24.21 (2013): 214003.

[15] Wurtz, Gregory A., et al. "Designed ultrafast optical nonlinearity in a plasmonic nanorod metamaterial enhanced by nonlocality." *Nature Nanotechnology* 6.2 (2011): 107.

[16] Cho, David J., et al. "Ultrafast modulation of optical metamaterials." *Optics Express* 17.20 (2009): 17652-17657.

[17] Green, Martin A., and Supriya Pillai. "Harnessing plasmonics for solar cells." *Nature Photonics* 6.3 (2012): 130.

[18] Wang, Yang, et al. "Metamaterial-plasmonic absorber structure for high efficiency amorphous silicon solar cells." *Nano Letters* 12.1 (2011): 440-445.

[19] Coppens, Zachary J., Ivan I. Kravchenko, and Jason G. Valentine. "Lithography‑free large‑area metamaterials for stable thermophotovoltaic energy conversion." *Advanced Optical Materials* 4.5 (2016): 671-676.

[20] Barber, D. J., and Ian C. Freestone. "An investigation of the origin of the colour of the Lycurgus Cup by analytical transmission electron microscopy." *Archaeometry* 32.1 (1990): 33-45.

[21] Freestone, Ian, et al. "The Lycurgus cup - a roman nanotechnology." *Gold Bulletin* 40.4 (2007): 270-277.

[22] Khurgin, Jacob B. "How to deal with the loss in plasmonics and metamaterials." *Nature Nanotechnology* 10.1 (2015): 2.

[23] Barnard, Edward S., et al. "Spectral properties of plasmonic resonator antennas." *Optics Express* 16.21 (2008): 16529-16537.

[24] Muehlschlegel, Peter, et al. "Resonant optical antennas." *Science* 308.5728 (2005): 1607-1609.

[25] Kim, Seungchul, et al. "High-harmonic generation by resonant plasmon field enhancement." *Nature* 453.7196 (2008): 757.

[26] Schuller, Jon A., et al. "Plasmonics for extreme light concentration and manipulation." *Nature Materials* 9.3 (2010): 193.

[27] Grober, Robert D., Robert J. Schoelkopf, and Daniel E. Prober. "Optical antenna: towards a unity efficiency near-field optical probe." *Applied Physics Letters* 70.11 (1997): 1354-1356.

[28] Crozier, K. B., et al. "Optical antennas: Resonators for local field enhancement." *Journal of Applied Physics* 94.7 (2003): 4632-4642.

[29] Schuck, P. J., et al. "Improving the mismatch between light and nanoscale objects with gold bowtie nanoantennas." *Physical Review Letters* 94.1 (2005): 017402.

[30] Farahani, Javad N., et al. "Single quantum dot coupled to a scanning optical antenna: a tunable superemitter." *Physical Review Letters* 95.1 (2005): 017402.

[31] Hu, Shuren, et al. "Experimental realization of deep-subwavelength confinement in dielectric optical resonators." *Science Advances* 4.8 (2018): eaat2355.

[32] Lohmüller, T., et al. "Single molecule tracking on supported membranes with arrays of optical nanoantennas." *Nano Letters* 12.3 (2012): 1717-1721.

[33] Roxworthy, Brian J., et al. "Reconfigurable nanoantennas using electron-beam manipulation." *Nature Communications* 5 (2014): 4427.

[34] Alu, Andrea, et al. "Epsilon-near-zero metamaterials and electromagnetic sources: Tailoring the radiation phase pattern." *Physical Review B* 75.15 (2007): 155410.

[35] Edwards, Brian, et al. "Experimental verification of epsilon-near-zero metamaterial coupling and energy squeezing using a microwave waveguide." *Physical Review Letters* 100.3 (2008): 033903.

[36] Marqués, Ricardo, et al. "Comparative analysis of edge-and broadside-coupled split ring resonators for metamaterial design-theory and experiments." *IEEE Transactions on Antennas and Propagation* 51.10 (2003): 2572-2581.

[37] Liu, Mengkun, et al. "Terahertz-field-induced insulator-to-metal transition in vanadium dioxide metamaterial." *Nature* 487.7407 (2012): 345.

[38] Yang, Yuanmu, et al. "Modulating the fundamental inductive-capacitive resonance in asymmetric double-split ring terahertz metamaterials." *Applied Physics Letters* 98.12 (2011): 121114.

[39] Oulton, Rupert F., et al. "Plasmon lasers at deep subwavelength scale." *Nature* 461.7264 (2009): 629.

[40] Boltasseva, Alexandra, and Harry A. Atwater. "Low-loss plasmonic metamaterials." *Science* 331.6015 (2011): 290-291.

[41] Xiao, Shumin, et al. "Loss-free and active optical negative-index metamaterials." *Nature* 466.7307 (2010): 735.

[42] Jahani, Saman, and Zubin Jacob. "All-dielectric metamaterials." *Nature Nanotechnology* 11.1 (2016): 23.

[43] Mie, Gustav. "Contributions to the optics of turbid media, particularly of colloidal metal solutions." *Transl. into ENGLISH from Ann. Phys.(Leipzig)*, 25. 3.1908 (1976):377-445.

[44] Lewin, L. "The electrical constants of a material loaded with spherical particles." *Journal of the Institution of Electrical Engineers-Part III: Radio and Communication Engineering* 94.27 (1947): 65-68.

[45] Moitra, Parikshit, et al. "Experimental demonstration of a broadband all-dielectric metamaterial perfect reflector." *Applied Physics Letters* 104.17 (2014): 171102.

[46] Holloway, Christopher L., et al. "A double negative (DNG) composite medium composed of magnetodielectric spherical particles embedded in a matrix." *IEEE Transactions on Antennas and Propagation* 51.10 (2003): 2596-2603.

[47] Huang, Xueqin, et al. "Dirac cones induced by accidental degeneracy in photonic crystals and zero-refractive-index materials." *Nature Materials* 10.8 (2011): 582.

[48] Moitra, Parikshit, et al. "Realization of an all-dielectric zero-index optical metamaterial." *Nature Photonics* 7.10 (2013): 791.

[49] Liu, Sheng, et al. "Optical magnetic mirrors without metals." *Optica* 1.4 (2014): 250-256.

[50] Esfandyarpour, Majid, et al. "Metamaterial mirrors in optoelectronic devices." *Nature Nanotechnology* 9.7 (2014): 542.

[51] Semouchkina, Elena, et al. "Sensing based on Fano-type resonance response of all-dielectric metamaterials." *Sensors* 15.4 (2015): 9344-9359.

[52] Yang, Yuanmu, et al. "All-dielectric metasurface analogue of electromagnetically induced transparency." *Nature Communications* 5 (2014): 5753.

[53] Arbabi, Amir, et al. "Dielectric metasurfaces for complete control of phase and polarization with subwavelength spatial resolution and high transmission." *Nature Nanotechnology* 10.11 (2015): 937.

[54] Khorasaninejad, Mohammadreza, et al. "Metalenses at visible wavelengths: Diffraction-limited focusing and subwavelength resolution imaging." *Science* 352.6290 (2016): 1190-1194.

[55] Kivshar, Yuri, and Andrey Miroshnichenko. "Meta-optics with Mie resonances." *Optics and Photonics News* 28.1 (2017): 24-31.

[56]   Slovick, Brian A., et al. "Metasurface polarization splitter." *Phil. Trans. R. Soc. A* 375.2090 (2017): 20160072.

[57]   Moitra, Parikshit, et al. "Large-scale all-dielectric metamaterial perfect reflectors." *ACS Photonics* 2.6 (2015): 692-698.

[58]   Bakker, Reuben M., et al. "Magnetic and electric hotspots with silicon nanodimers." *Nano Letters* 15.3 (2015): 2137-2142.

[59]   Yang, Yuanmu, et al. "Nonlinear Fano-resonant dielectric metasurfaces." *Nano Letters* 15.11 (2015): 7388-7393.

[60]   Wu, Chihhui, et al. "Spectrally selective chiral silicon metasurfaces based on infrared Fano resonances." *Nature Communications* 5 (2014): 3892.

[61]   Wang, Wenyi, et al. "Enhanced absorption in two-dimensional materials via Fano-resonant photonic crystals." *Applied Physics Letters* 106.18 (2015): 181104.

[62]   Piper, Jessica R., and Shanhui Fan. "Total absorption in a graphene monolayer in the optical regime by critical coupling with a photonic crystal guided resonance." *ACS Photonics* 1.4 (2014): 347-353.

[63]   Zheludev, Nikolay I., and Yuri S. Kivshar. "From metamaterials to metadevices." *Nature Materials* 11.11 (2012): 917.

[64]   Fan, Kebin, and Willie J. Padilla. "Dynamic electromagnetic metamaterials." *Materials Today* 18.1 (2015): 39-50.

[65]   Phare, Christopher T., et al. "Graphene electro-optic modulator with 30 GHz bandwidth." *Nature Photonics* 9 (8) (2015): 511-514.

[66]   Liu, M., et al. "A graphene-based broadband optical modulator." *Nature*, 474.7349 (2011): 64-67.

[67]   Li, W., et al. "Ultrafast all-optical graphene modulator." *Nano Letters*, 14.2(2014):955-959.

[68] Huang, Yao-Wei, et al. "Gate-tunable conducting oxide metasurfaces." *Nano Letters* 16.9 (2016): 5319-5325.

[69] Abb, Martina, et al. "All-optical control of a single plasmonic nanoantenna–ITO hybrid." *Nano Letters* 11.6 (2011): 2457-2463.

[70] Chen, Chi-Fan, et al. "Controlling inelastic light scattering quantum pathways in graphene." *Nature* 471.7340 (2011): 617-620.

[71] Emani, Naresh K., et al. "Electrically tunable damping of plasmonic resonances with graphene." *Nano Letters* 12.10 (2012): 5202-5206.

[72] Emani, Naresh K., et al. "Electrical modulation of Fano resonance in plasmonic nanostructures using graphene." *Nano Letters* 14.1 (2013): 78-82.

[73] Lee, C. C., et al. "Broadband graphene electro-optic modulators with sub-wavelength thickness." *Optics Express* 20.5 (2012): 5264-5269.

[74] Liu, Ming, et al. "A graphene-based broadband optical modulator." *Nature* 474.7349 (2011): 64.

[75] Li, Wei, et al. "Ultrafast all-optical graphene modulator." *Nano Letters* 14.2 (2014): 955-959.

[76] Huang, Yao-Wei, et al. "Gate-tunable conducting oxide metasurfaces." *Nano Letters* 16.9 (2016): 5319-5325.

[77] Shrekenhamer, David, Wen-Chen Chen, and Willie J. Padilla. "Liquid crystal tunable metamaterial absorber." *Physics Review Letters* 110.17 (2013): 177403.

[78] Zhao, Yanhui, et al. "Light-driven tunable dual-band plasmonic absorber using liquid-crystal-coated asymmetric nanodisk array." *Applied Physics Letters* 100.5 (2012): 053119.

[79] Xiao, S. M. et al. "Tunable magnetic response of metamaterials." *Applied Physics Letters* 95 (2009): 033115.

[80] Kang, B. et al. "Optical switching of near infrared light transmission in metamaterial-liquid crystal cell structure." *Optics Express* 18 (2010): 16492–16498.

[81] Ou, Jun-Yu, et al. "Reconfigurable photonic metamaterials." *Nano Letters* 11.5 (2011): 2142-2144.

[82] Ou, Jun-Yu, et al. "An electromechanically reconfigurable plasmonic metamaterial operating in the near-infrared." *Nature Nanotechnology* 8.4 (2013): 252-255.

[83] Chen, Hou-Tong, et al. "Active terahertz metamaterial devices." *Nature* 444.7119 (2006): 597.

[84] Tao, Hu, et al. "MEMS based structurally tunable metamaterials at terahertz frequencies." *Journal of Infrared, Millimeter, and Terahertz Waves* 32.5 (2011): 580-595.

[85] Dicken, Matthew J., et al. "Frequency tunable near-infrared metamaterials based on VO_2 phase transition." *Optics Express* 17.20 (2009): 18330-18339.

[86] Zhang, Shuang, et al. "Photoinduced handedness switching in terahertz chiral metamolecules." *Nature Communications* 3 (2012): 942.

[87] Sterl, Florian, et al. "Magnesium as novel material for active plasmonics in the visible wavelength range." *Nano Letters* 15.12 (2015): 7949-7955.

[88] Rahmani, Mohsen, et al. "Reversible thermal tuning of all‐dielectric metasurfaces." *Advanced Functional Materials* 27.31 (2017): 1700580.

[89] Su, Zhaoxian, et al. "Electrically tunable metasurface based on Mie-type dielectric resonators." *Scientific Reports* 7 (2017): 43026.

[90] Gutruf, Philipp, et al. "Mechanically tunable dielectric resonator metasurfaces at visible frequencies." *ACS Nano* 10 (1): 133-141 (2015).

[91] Sautter, J., Staude, et al. "Active tuning of all-dielectric metasurfaces." *ACS Nano* 9 (4): 4308-4315 (2015).

[92] Parry, Matthew, et al. "Active tuning of high-Q dielectric metasurfaces." *Applied Physics Letters* 111.5 (2017): 053102.

[93] Bohn, Justus, et al. "Active tuning of spontaneous emission by Mie-resonant dielectric metasurfaces." *Nano Letters* 18.6 (2018): 3461-3465.

[94] Komar, Andrei, et al. "Dynamic beam switching by liquid crystal tunable dielectric metasurfaces." *ACS Photonics* 5.5 (2018): 1742-1748.

[95] Komar, Andrei, et al. "Electrically tunable all-dielectric optical metasurfaces based on liquid crystals." *Applied Physics Letters* 110.7 (2017): 071109.

[96] Shcherbakov, Maxim R., et al. "Ultrafast all-optical tuning of direct-gap semiconductor metasurfaces." *Nature Communication* 8 (2017).17

[97] Jiang, Li-Hua, et al. "Tunable terahertz filters based on graphene plasmonic all-dielectric metasurfaces." *Plasmonics* 13.2 (2018): 525-530.

[98] Iyer, P. P., et al. "Ultrawide thermal free-carrier tuning of dielectric antennas coupled to epsilon-near-zero substrates." *Nature Communication* 8.1(2017), 472.

[99] Howes, Austin, et al. "Dynamic transmission control based on all-dielectric Huygens metasurfaces." *Optica* 5.7 (2018): 787-792.

[100] Liu, Tingting, et al. "Active control of electromagnetically induced transparency analogue in all-dielectric metamaterials loaded with graphene." arXiv preprint arXiv:1808.07242 (2018).

[101] Forouzmand, Ali, et al. "A tunable multigate indium‐tin‐oxide‐assisted all‐dielectric metasurface." *Advanced Optical Materials* 6.7 (2018): 1701275.

[102] Arezoomandan, Sara, et al. "Graphene-dielectric integrated THz metasurfaces." *Semiconductor Science and Technology* (2018).

[103] Iyer, Prasad P., et al. "Ultrawide thermal free-carrier tuning of dielectric antennas coupled to epsilon-near-zero substrates." *Nature Communications* 8.1 (2017): 472.

[104] Sun, Shang, et al. "Real-time tunable colors from microfluidic reconfigurable all-dielectric metasurfaces." *ACS Nano* 12.3 (2018): 2151-2159.

[105] Arbabi, Ehsan, et al. "MEMS-tunable dielectric metasurface lens." *Nature Communications* 9.1 (2018): 812.

[106] Kubytskyi, Viacheslav, Svend-Age Biehs, and Philippe Ben-Abdallah. "Radiative bistability and thermal memory." *Physical Review Letters* 113.7 (2014): 074301.

[107] Driscoll, Tom, et al. "Memory metamaterials." *Science* 325.5947 (2009): 1518-1521.

[108] Zhu, Zhihua, et al. "Dynamically reconfigurable metadevice employing nanostructured phase-change materials." *Nano Letters* 17.8 (2017): 4881-4885.

[109] Wang, H., Yang, Y., & Wang, L. "Switchable wavelength-selective and diffuse metamaterial absorber/emitter with a phase transition spacer layer." *Applied Physics Letters* 105.7 (2014): 071907.

[110] Cueff, S., et al. "Dynamic control of light emission faster than the lifetime limit using VO_2 phase-change" *Nature Communication* 6(2015): 8636.

[111] Kats, Mikhail A., et al. "Ultra-thin perfect absorber employing a tunable phase change material." *Applied Physics Letters* 101.22 (2012): 221101.

[112] Kim, Minseok, et al. "Vanadium-dioxide-assisted digital optical metasurfaces for dynamic wavefront engineering." *JOSA B* 33.5 (2016): 980-988.

[113] Michel, Ann-Katrin U., et al. "Using low-loss phase-change materials for mid-infrared antenna resonance tuning." *Nano Letters* 13.8 (2013): 3470-3475.

[114] Peng, Xiao-Yu, et al. "Active near infrared linear polarizer based on VO_2 phase transition." *Journal of Applied Physics* 114.16 (2013): 163103.

[115] L. Liu, et al. "Hybrid metamaterials for electrically triggered multifunctional control." *Nature Communication* 7 (2016): 13236.

[116] Zhou, You, et al. "Voltage-triggered ultrafast phase transition in vanadium dioxide switches." *IEEE Electron Device Letters* 34.2 (2013): 220-222.

[117] Wang, Dacheng, et al. "Switchable ultrathin quarter-wave plate in terahertz using active phase-change metasurface." *Scientific Reports* 5 (2015): 15020.

[118] Dicken, Matthew J., et al. "Frequency tunable near-infrared metamaterials based on VO_2 phase transition." *Optics Express* 17.20 (2009): 18330-18339.

[119] Ferrara, Davon W., et al. "Plasmonic probe of the semiconductor to metal phase transition in vanadium dioxide." *Nano Letters* 13.9 (2013): 4169-4175.

[120] Wang, Xi, et al. "All-solid-state tunable Bragg filters based on a phase transition material." *CLEO:Science and Innovations*. Optical Society of America, 2017.

[121] Ollanik, Adam, et al. "Dynamically tunable, vanadium dioxide Huygens source metasurfaces." *CLEO: QELS Fundamental Science*. Optical Society of America, 2017.

[122] Tian, Jingyi, et al. "Reconfigurable all-dielectric antenna-based metasurface driven by multipolar resonances." *Optics Express* 26.18 (2018): 23918-23925.

[123] Abdollahramezani, Sajjad, et al. "Dynamic dielectric metasurfaces incorporating phase-change material." *CLEO: Science and Innovations*. Optical Society of America, 2018.

[124] Verleur, Hans W., A. S. Barker Jr, and C. N. Berglund. "Optical properties of VO_2 between 0.25 and 5 eV." *Physical Review* 172.3 (1968): 788.

[125] Yang, Zheng, Changhyun Ko, and Shriram Ramanathan. "Oxide electronics utilizing ultrafast metal-insulator transitions." *Annual Review of Materials Research* 41 (2011): 337-367.

[126] Guerin, Samuel, et al. "Synthesis and screening of phase change chalcogenide thin film materials for data storage." *ACS Combinatorial Science* 19.7 (2017): 478-491.

[127] Kolobov, Alexander V., et al. "Understanding the phase-change mechanism of rewritable optical media." *Nature Materials* 3.10 (2004): 703.

[128] Zheng, Jianyun, Shanhu Bao, and Ping Jin. "$TiO_2(R)/VO_2(M)/TiO_2(A)$ multilayer film as smart window: Combination of energy-saving, antifogging and self-cleaning functions." *Nano Energy* 11 (2015): 136-145.

[129] Gao, Yanfeng, et al. "Nanoceramic VO_2 thermochromic smart glass: A review on progress in solution processing." *Nano Energy* 1.2 (2012): 221-246.

[130] Wang, Qian, et al. "Optically reconfigurable metasurfaces and photonic devices based on phase change materials." *Nature Photonics* 10.1 (2016): 60.

[131] Li, Peining, et al. "Reversible optical switching of highly confined phonon–polaritons with an ultrathin phase-change material." *Nature Materials* 15.8 (2016): 870.

[132] Liang, Jiran, et al. "Room temperature CH_4 sensing properties of Au decorated VO_2 nanosheets." *Materials Letters* 184 (2016): 92-95.

[133] Strelcov, Evgheni, Yigal Lilach, and Andrei Kolmakov. "Gas sensor based on metal−insulator transition in VO_2 nanowire thermistor." *Nano Letters* 9.6 (2009): 2322-2326.

[134] Simo, Aline, et al. "VO_2 nanostructures based chemiresistors for low power energy consumption hydrogen sensing." *International Journal of Hydrogen Energy* 39.15 (2014): 8147-8157.

[135] Wuttig, Matthias, and Noboru Yamada. "Phase-change materials for rewriteable data storage." *Nature Materials* 6.11 (2007): 824.

[136] Lankhorst, Martijn HR, Bas WSMM Ketelaars, and Robertus AM Wolters. "Low-cost and nanoscale non-volatile memory concept for future silicon chips." *Nature Materials* 4.4 (2005): 347.

[137] Pouget, J. P., et al. "Electron localization induced by uniaxial stress in pure VO_2." *Physical Review Letters* 35.13 (1975): 873.

[138] Pouget, J. P., et al. "Dimerization of a linear Heisenberg chain in the insulating phases of $V_{1-x}Cr_xO_2$." *Physical Review B* 10.5 (1974): 1801.

[139] Lazarovits, Bence, et al. "Effects of strain on the electronic structure of VO_2." *Physical Review B* 81.11 (2010): 115117.

[140] Zhang, Hai-Tian, et al. "Wafer-scale growth of VO_2 thin films using a combinatorial approach." *Nature Communications* 6 (2015): 8475.

[141] Haverkort, M. W., et al. "Orbital-assisted metal-insulator transition in VO_2." *Physical Review Letters* 95.19 (2005): 196404.

[142] Wang, Hongchen, Xinjian Yi, and Yi Li. "Fabrication of VO_2 films with low transition temperature for optical switching applications." *Optics Communications* 256.4-6 (2005): 305-309.

[143] Beteille, F., and J. Livage. "Optical switching in VO_2 thin films." *Journal of Sol-Gel Science and Technology* 13.1-3 (1998): 915-921.

[144] Miller, Kevin J., et al. "Silicon waveguide optical switch with embedded phase change material." *Optics Express* 25.22 (2017): 26527-26536.

[145] Miller, Kevin J., Richard F. Haglund, and Sharon M. Weiss. "Optical phase change materials in integrated silicon photonic devices." *Optical Materials Express* 8.8 (2018): 2415-2429.

[146] Huang, Zhangli, et al. "Infrared characteristics of VO_2 thin films for smart window and laser protection applications." *Applied Physics Letters* 101.19 (2012): 191905.

[147] Stefanovich, G., A. Pergament, and D. Stefanovich. "Electrical switching and Mott transition in VO_2." *Journal of Physics: Condensed Matter* 12.41 (2000): 8837.

[148] Kim, Hyun-Tak, et al. "Mechanism and observation of Mott transition in VO_2-based two- and three-terminal devices." *New Journal of Physics* 6.1 (2004): 52.

[149] Jones, William; March, Norman H. (1985). Theoretical Solid State Physics. Courier Dover Publications. ISBN 0-486-65016-2.

[150] He, Xinfeng, et al. "In situ atom scale visualization of domain wall dynamics in VO_2 insulator-metal phase transition." *Scientific Reports* 4 (2014): 6544.

[151] Pan, Mei, et al. "Raman study of the phase transition in VO_2 thin films." *Journal of Crystal Growth* 268.1-2 (2004): 178-183.

[152] Case, Francine C. "Crystallographic transition in conventional bronze and anomalous blue VO_2 thin films." *Applied Optics* 28.14 (1989): 2731-2735.

[153] Zhang, Dong-ping, et al. "High performance VO_2 thin films growth by DC magnetron sputtering at low temperature for smart energy efficient window application." *Journal of Alloys and Compounds* 659 (2016): 198-202.

[154] Wen, Haidan, et al. "Structural and electronic recovery pathways of a photoexcited ultrathin VO_2 film." *Physical Review B* 88.16 (2013): 165424.

[155] Oh, Dong-Wook, et al. "Thermal conductivity and dynamic heat capacity across the metal-insulator transition in thin film VO_2." *Applied Physics Letters* 96.15 (2010): 151906.

[156] Berglund, C. N., and H. J. Guggenheim. "Electronic properties of VO_2 near the Semiconductor-Metal Transition." *Physical Review* 185.3 (1969): 1022.

[157] Markov, Petr, et al. "Optically monitored electrical switching in VO_2." *ACS Photonics* 2.8 (2015): 1175-1182.

[158] Wegkamp, Daniel, et al. "Instantaneous band gap collapse in photoexcited monoclinic VO_2 due to photocarrier doping." *Physical Review Letters* 113.21 (2014): 216401.

[159] Kumar, Sunil, Francis Maury, and Naoufal Bahlawane. "Electrical switching in semiconductor-metal self-assembled VO_2 disordered metamaterial coatings." *Scientific Reports* 6 (2016): 37699.

[160] Currie, Marc, Michael A. Mastro, and Virginia D. Wheeler. "Characterizing the tunable refractive index of vanadium dioxide." *Optical Materials Express* 7.5 (2017): 1697-1707.

[161] Kozen, Alexander C., et al. "Structural characterization of atomic layer deposited vanadium dioxide." *The Journal of Physical Chemistry C* 121.35 (2017): 19341-19347.

[162] Marvel, Robert E., et al. "Influence of deposition process and substrate on the phase transition of vanadium dioxide thin films." *Acta Materialia* 91 (2015): 217-226.

[163] Muraoka, Y., and Z. Hiroi. "Metal–insulator transition of VO_2 thin films grown on TiO_2 (001) and (110) substrates." *Applied Physics Letters* 80.4 (2002): 583-585.

[164] Lopez, Rene, et al. "Size effects in the structural phase transition of VO_2 nanoparticles." *Physical Review B* 65.22 (2002): 224113.

[165] Donev, E. U., et al. "Size effects in the structural phase transition of VO_2 nanoparticles studied by surface-enhanced Raman scattering." *Journal of Optics A: Pure and Applied Optics* 11.12 (2009): 125002.

[166] Lopez, Rene, Leonard C. Feldman, and Richard F. Haglund Jr. "Size-dependent optical properties of VO_2 nanoparticle arrays." *Physical Review Letters* 93.17 (2004): 177403.

[167] Wang, Lei, Shu-Ren Lu, and Jing Wen. "Recent advances on neuromorphic systems using phase-change materials." *Nanoscale Research Letters* 12.1 (2017): 347.

[168] Simpson, R. E., et al. "Interfacial phase-change memory." *Nature Nanotechnology* 6.8 (2011): 501.

[169] Ee, Ho-Seok, and Ritesh Agarwal. "Tunable metasurface and flat optical zoom lens on a stretchable substrate." *Nano Letters* 16.4 (2016): 2818-2823.

[170] Tittl, Andreas, et al. "A switchable mid‐infrared plasmonic perfect absorber with multispectral thermal imaging capability." *Advanced Materials* 27.31 (2015): 4597-4603.

[171] Kivshar, Yuri. "All-dielectric meta-optics and non-linear nanophotonics." *National Science Review* 5.2 (2018): 144-158.

[172] Decker, Manuel, et al. "High‐efficiency dielectric Huygens' surfaces." *Advanced Optical Materials* 3.6 (2015): 813-820.

[173] Pfeiffer, Carl, and Anthony Grbic. "Metamaterial Huygens' surfaces: tailoring wave fronts with reflectionless sheets." *Physical Review Letters* 110.19 (2013): 197401.

[174] Liu, K., et al. "Giant-amplitude, high-work density microactuators with phase transition activated nanolayer bimorphs." *Nano Letters* 12.12 (2012): 6302-6308.

[175] Yamin, Tony, Yakov M. Strelniker, and Amos Sharoni. "High resolution Hall measurements across the VO_2 metal-insulator transition reveal impact of spatial phase separation." *Scientific Reports* 6 (2016): 19496.

[176] Tadjer, Marko J., et al. "Temperature and electric field induced metal-insulator transition in atomic layer deposited VO_2 thin films." *Solid-State Electronics* 136 (2017): 30-35.

[177] Borneman J. D. "Optical metamaterials: linear and nonlinear characterization and application to optical limiting[D]". Purdue University, 2010.

[178] Lin H. B., Tonucci R. J., Campillo A. J. "Two-dimensional photonic bandgap optical limiter in the visible." *Optics Letters* 23.2 (1998): 94-96.

[179] Bao Q., et al. "Graphene nanobubbles: a new optical nonlinear material." *Advanced Optical Materials,* 3.6 (2015): 744-749.

[180] Lim G. K., et al. "Giant broadband nonlinear optical absorption response in dispersed graphene single sheets." *Nature Photonics* 5.9 (2011): 554-560.

[181] MacChesney, J. B., & Guggenheim, H. J. "Growth and electrical properties of vanadium dioxide single crystals containing selected impurity ions." *Journal of Physics and Chemistry of Solids* 30.2 (1969): 225-234.

[182] Jorgenson, G. V., & Lee, J. C. "Doped vanadium oxide for optical switching films." *Solar Energy Materials* 14 (3-5) (1986): 205-214.

[183] Campione, Salvatore, Igal Brener, and Francois Marquier. "What is an epsilon-near-zero mode?" *Integrated Photonics Research, Silicon and Nanophotonics*. Optical Society of America, 2015.

[184] Yoon, Junho, et al. "Broadband epsilon-near-zero perfect absorption in the near-infrared." *Scientific Reports* 5 (2015): 12788.

[185] Vassant, Simon, et al. "Berreman mode and epsilon near zero mode." *Optics Express* 20.21 (2012): 23971-23977.

[186] Vassant, Simon, et al. "Epsilon-near-zero mode for active optoelectronic devices." *Physical Review Letters* 109.23 (2012): 237401.

[187] Braun, Johannes M., et al. "Ultrafast response of photoexcited carriers in VO_2 at high-pressure." *New Journal of Physics* 20.8 (2018): 083003.

[188] Johnson, Peter B., and R. W. Christy. "Optical constants of the noble metals." *Physical Review B* 6.12 (1972): 4370.

[189] Thornton, John A., and D. W. Hoffman. "Stress-related effects in thin films." *Thin Solid Films* 171.1 (1989): 5-31.